Femtosecond Gain-Index Coupling in Femtosecond Nonlinearity Measurements of InGaAsP Diode Laser Amplifiers

by

Erik R. Thoen

B.S. Engineering, Swarthmore College (1995)

Submitted to the Department of Electrical Engineering and Computer Science in partial fulfillment of the requirements for the degree of

Master of Science

at the

MASSACHUSETTS INSTITUTE OF TECHNOLOGY

February, 1997

Signature of Author . . . .
Department of Electrical Engineering and Computer Science
February, 1997

Certified by . . . .
Erich P. Ippen
Thesis Supervisor

Accepted by . . . .
Arthur C. Smith
Chair, Department Committee on Graduate Students

Femtosecond Gain-Index Coupling in Femtosecond Nonlinearity Measurements of InGaAsP Diode Laser Amplifiers

by

Erik R. Thoen

Submitted to the Department of Electrical Engineering and Computer Science in partial fulfillment of the requirements for the degree of

Master of Science

Abstract

New theory on measuring gain and index changes in femtosecond pump probe studies suggests a spectral artifact is present which may have obscured the ultrafast response in previous studies of InGaAsP laser diode amplifiers. A femtosecond heterodyne pump-probe technique is implemented using an Erbium-doped stretched-pulse mode-locked fiber laser centered at 1.55 μm and used to obtain simultaneous measurements of transmission and phase changes. These results are analyzed considering the spectral artifact and an experimental scheme for eliminating the artifact is discussed.

Thesis Supervisor: Erich P. Ippen
Title: Elihu Thomson Professor of Electrical Engineering and Physics

ACKNOWLEDGMENTS

It has been a great pleasure to perform this work under the guidance of Professor Erich P. Ippen. I could not have found a better advisor. All too often people will attempt to overwhelm you with equations and obtuse mathematics, but he always has an equally accurate yet profoundly simple means of considering physical processes. His direction and constant patience in explaining every detail to me has been essential in making this research rewarding. I look forward to working for him in the coming years; they are sure to be exciting.

I thank Professor Haus for initially sparking my interest in this group and offering me a possible research project in the group. He continues to keep me on my toes with his ability to pick me for a group talk when I least expect it. And of course to Cindy Kopf, Donna Gale, and Mary Aldridge who all keep the group running both in terms of stationary supplies and juicy gossip.

Collaborators from outside of the optics group have also made this thesis possible. Initially Dr. Gadi Lenz at Lucent Technologies was just a phone call away, willing to answer questions about strange things I kept finding around the lab. Dr. Katie Hall at Lincoln Laboratory loaned me a number of key pieces of equipment, and has been a great help in interpreting results and making suggestions on improving the experimental techniques. Dr. Joe Donnelly, also at Lincoln Laboratory, a long time friend, supplied the devices for the experiment, as well as his wonderful ability to tell me more about something than I ever sought to know.

Several members of the group have been especially helpful. Dr. Günter Steinmeyer has been a fantastic lab mentor. I have been a great beneficiary of his very didactic approach. In fact, I now know more about color center lasers than I could ever possibly use. I thank Siegfried Fleischer, as an office-mate and circuit guru, for having the patience to deal with a constant stream of novice circuit questions. I can only hope to aspire to Dave Dougherty's deep understanding of the theory of the devices and the techniques used in the study of in these devices, and I thank him for imparting so much of his knowledge to me. Lynne Nelson helped me with prism compression on more than one occasion, and she and David Jones both assisted me in rebuilding the fiber laser. And of course everyone else in the group deserves mention including Pat Chou (for that crazy label maker and Dim Sum with Suky), Matt Grein (for being an officemate), Dr. Brent Little (for being a good TA), Dr. Stefano Longhi, Dr. Moti Margalit, Dr. Masayuki Matsumoto, Christina Manolatou, Dr. Shu Namiki, Dr. Dominique Peter, Costas Tziligakis, William Wong, Charles Yu, the recently graduated Luc Boivin, Jay Damask, Farzana Khatri, and the Fujimoto contingent of Igor Bilinsky, Steve Boppart, Dr. Brett Bouma, Boris Golubovic, Costas Pitras, and Dr. Gary Tearney.

Of course outside of the lab, I owe may thanks to quite a number of close friends. I thank my very best friend Kaori Shingledecker for putting up with this thesis for way to long and making sure I kept sane. She's the one that keeps me going. Of course I must thank my apartmentmate Tom Murphy, or he may stop paying his portion of the rent. Also, I owe him dinner. Both of them have assisted me in proofreading this document, so any corrections can be forwarded to them. I also thank James Hockenberry, a fellow Swattie, for the many opportunities to recall old times and make fun of new ones.

And finally I thank God for making all things possible. Especially for blessing me with parents who have watched over me, encouraged me, supported me in everything I do, and generally been pretty awesome. Without their love, I wouldn't be here.

TABLE OF CONTENTS

CHAPTER 1: INTRODUCTION

Measurements of femtosecond nonlinearities in diode lasers have been made in the wave-length regime of 1.5 μm using pump-probe techniques in the time domain [3] and four wave mixing techniques in the frequency domain [7]. The generation of femtosecond pulses at 1.5 μm is a significant obstacle to time domain studies; to date, color center lasers have been used almost exclusively. The technical obstacles of cryogenic cooling, high vacuum, and active stabilization make them unstable and difficult laser system to operate. However, recently the stretched-pulse fiber laser has been shown to produce sufficiently high output powers for time-resolved measurement applications and pulses compressed to durations less than 100 fs at 1.5 μm [48]. Additionally, the source is pumped with a solid state Master Oscillator Power Amplifier (MOPA) diode laser and has very little amplitude or phase jitter. These qualities make it an ideal source for time-resolved experiments.

Recent theoretical advances suggest that coupling between index and gain dynamics in a pump-probe experiment on a femtosecond time scale contributes significantly to the response of semiconductor optical amplifiers [35]. Experimental verification of this theory requires systematic measurements of both index and gain changes. A heterodyne pump-probe system is ideal for measuring the index changes as well as adding the ability to arbitrarily choose the pump and probe polarizations. Additionally, direct comparison of index and gain responses requires careful measurements of zero time delay.

Here we outline experimental results we obtained to further characterize the spectral artifact and possible methods of eliminating it from measurements. We begin in Chapter 2 by developing a simple model of gain in semiconductors based on rate equations. We consider how such a model predicts the effect on transmission and phase of various ultrafast processes occurring in semiconductor devices. Then we consider the theory of pump-probe measurements of both transmission and phase of collinear devices. Finally we give special consideration to artifacts produced both by coherence between the pump and probe beams and the spectral filtering produced by the gain slope.

In Chapter 3 we outline the experimental design for the heterodyne technique using the stretched-pulse erbium-doped modelocked fiber laser. We consider the typical operating characteristics of the laser, outline pulse compression techniques, and discuss one method of spectral filtering. We demonstrate the relatively large wavelength tunability of the source using an interference filter, and compare it to other sources available at the same wavelength. Finally we discuss the details of the heterodyne pump-probe system for this particular laser.

In Chapter 4 we present the results of a complete study of a particular multiple quantum well (MQW) semiconductor optical amplifier (SOA). Initially we consider the bias-lead monitoring technique as a diagnostic for the system. We discuss briefly the general characteristics of the particular MQW devices studied and the linearity regimes required for reasonable pump-probe results. Then we present the data obtained for all polarization combinations in gain, transparency, and absorption regimes of the device. Finally we discuss the influence of the spectral artifact and the deficiencies of the fitting routines used to fit the data.

We discuss the methods for eliminating the spectral artifact in Chapter 5. We present initial experimental measurements of the gain slope which should govern the influence of the spectral artifact on the data. Then we consider an interference filter as one means of linear filtering to eliminate the spectral artifact.

We finish the thesis with a discussion of meaningful conclusions which can be drawn from the results presented here. Several simple steps can be taken to improve our understanding of the spectral artifact and carefully quantify how important the spectral artifact is to understanding data obtained from virtually any pump-probe experiment.

CHAPTER 2: PUMP-PROBE OF SEMICONDUCTORS

For this thesis, we use a pump-probe technique to measure the change in gain and index in a semiconductor multiple quantum well (MQW) optical amplifier as a function of time to determine the rates of various ultrafast processes. Although a number of theorists have performed full density matrix calculations of the various processes occurring in such devices, a simple model of gain and index in bulk semiconductors is sufficient to provide significant physical intuition for the results we present [1, 2]. We also consider the theory of pump-probe measurements and propose a phenomenological model for fitting the experimental data which we present in a later chapter.

2.1   Gain in Semiconductors

We model a diode laser as a simple two-energy-level system, where the number of electrons in each of the two states governs the transition probability. When the number of electrons in the lower energy level E_1 is higher than the number in the higher energy level E_2, the diode is more likely to absorb an incident photon with energy equal to E_2 - E_1 than to emit an additional photon. In the reverse case, where the number of electrons in E_2 is higher than in E_1 emission is more probable. The result is quite intuitive, but the mathematics can serve to generate a quantitative result.

In the two level system with electronic levels E_1 and E_2, we can write the rate of stimulated emission, or the rate of a electron moving from the upper level to the lower level and releasing a photon, as

$$r_{21} = \gamma f_c (1 - f_v) P(E_{21}),$$

(2.1)

where γ is the transition probability, f_c is the number of electrons in the upper level, f_v is the number of electrons in the lower level, and $P(E_{21})$ is the density of photons with energy E_{21} where

$$E_{21} = E_2 - E_1 . \qquad (2.2)$$

Similarly the rate of stimulated absorption, or the rate of electrons moving from the lower level to the upper level with the absorption of a photon, is given by

$$r_{12} = \gamma f_v (1 - f_c) P(E_{21}) . \qquad (2.3)$$

It is well known from the Einstein relations that γ is the same in both equations. Summing the two rates gives the total rate of stimulated emission

$$r_{tot} = r_{21} - r_{12} = \gamma (f_c - f_v) P(E_{21}) . \qquad (2.4)$$

The gain is then the total stimulated emission rate divided by the input photon rate, or

$$g(E_{21}) = \frac{r_{tot}}{P(E_{21}) v_g} = \gamma \frac{n}{c} (f_c - f_v) \qquad (2.5)$$

where v_g is the group velocity and is equal to c/n, where c is the speed of light, and n is the refractive index. From this expression, we can easily see the that sign of the gain will be governed by the relative carrier density in the two levels.

For semiconductor diodes, the gain is slightly more complicated because instead of just two electronic states, there is distribution of states in both valence and conduction bands and the probability of the sum of states must be considered. The density of states for a bulk semiconductor diode can be derived from first principles [8]. The lattice structure of the semiconductor may be modeled as a simple 3-D infinite wall box. By separation of variables, the solution to Schrödinger's equation for a 3-D box of dimension L, is simply a multiplication of the well known result for a 1-D box

$$\Psi = A \sin(k_x x) \sin(k_y y) \sin(k_z z), \qquad (2.6)$$

where Ψ is the wavefunction, and each k_i is defined from the boundary conditions as

$$k_i = n_i \frac{\pi}{L} \qquad (2.7)$$

where n_i is a positive integer denoting a state. Using this result, the energy is written

$$E = \frac{1}{8m} \left(\frac{h}{L} \right)^2 (n_x^2 + n_y^2 + n_z^2), \qquad (2.8)$$

where h is Planck's constant and m is the electron mass. The total number of states are obtained through an integration in k-space. The differential in k-space can be obtained using Equation 2.7 to write

$$dN = \frac{d^3k}{\left(\dfrac{\pi}{L}\right)^3} = \frac{V}{\pi^3}d^3k,$$ (2.9)

where V is the volume of the differential. The total number of states is then given by

$$N = 2 \iiint_{k>0, k<k_F} \frac{V}{\pi^3}d^3k,$$ (2.10)

where k_F is the Fermi wavenumber. The integral is simplified by using spherical coordinates and recognizing it is simply an integral of one-eighth of a sphere since all n_i are positive integers. Solving for the density per unit volume gives

$$n = \frac{N}{V} = \frac{1}{\pi^2}\int_0^{k_F} k^2 dk.$$ (2.11)

Performing the integral gives

$$n = \frac{k_F^3}{3\pi^2}.$$ (2.12)

Using this result, we write Equation 2.8 in terms of energy and substitute for

$$n = \frac{\left(\dfrac{2\pi\sqrt{2mE_F}}{h}\right)^3}{3\pi^2} = \frac{1}{3\pi^2}\left(\frac{8m\pi^2}{h^2}\right)^{3/2} E^{3/2}.$$ (2.13)

Then the density of states, ρ, written for all energy is simply

$$\rho = \frac{\partial n}{\partial E} = \frac{1}{2\pi^2}\left(\frac{8m\pi^2}{h^2}\right)^{3/2} E^{1/2}.$$ (2.14)

By evaluating the general expression for the density of states at the appropriate energies, the expressions for the density of states in the conduction and valence bands are

$$\rho_c(E - E_c) = \frac{1}{2\pi^2}\left(\frac{8m_c\pi^2}{h^2}\right)^{3/2}(E - E_c)^{1/2}$$ (2.15)

$$\rho_v(E_v - E) = \frac{1}{2\pi^2}\left(\frac{8m_v\pi^2}{h^2}\right)^{3/2}(E_v - E)^{1/2},$$ (2.16)

where E_c is the energy of the conduction band edge, m_c is the effective mass of electrons in the conduction band, E_v is the energy of the valence band edge, and m_v is the effective mass of electrons in the

valence band. For 2-D multiple quantum well (MQW) structures, the density of states changes in discrete steps under the envelope of the 3-D density of states derived here [9]. Although the density of states is slightly different, the theory presented here is sufficiently accurate to provide a simple physical model.

The expressions for the density of states only indicate the states that are available; the Fermi distribution function gives the probability that a particular energy state, E, is occupied. For the conduction band the Fermi function is

$$f_c(E, T_c) = \frac{1}{1 + e^{(E - \mu_c)/k_b T_c}},$$ (2.17)

where T_c is the temperature of electrons in the conduction band, μ_c is the quasi-Fermi energy for electrons in the conduction band, and k_b is Boltzmann's constant. Similarly, the probability of an electron in a particular energy state in the valence band is given by

$$f_v(E, T_v) = \frac{1}{1 + e^{(E - \mu_v)/k_b T_v}},$$ (2.18)

where T_v is the temperature of the electrons in the valence band and μ_v is the quasi-Fermi energy for electrons in the valence band. Since dynamics are often understood in terms of holes in the valence band, we may write the occupation probability for holes is $1 - f_v$.

Combining the probability densities and the density of states in each band, the electron density is given by

$$N = \int_{-\infty}^{\infty} \rho_c(E - E_c) f_c(E, T_c) dE,$$ (2.19)

where N is the density of electrons in the conduction band. Similarly, for holes in the valence band

$$P = \int_{-\infty}^{\infty} \rho_v(E_v - E)(1 - f_v(E, T_v)) dE,$$ (2.20)

where P is the density of holes in the valence band. These two equations are often used to solve numerically for the quasi-Fermi levels μ_c and μ_v because the other parameters are known. Figure 2.1 shows the density of states and electron and hole densities calculated using the expressions above for parameters typical of a long-wavelength InGaAsP diode laser.

Now that we have calculated expressions for the densities in the upper and lower bands, we can return to the expression for the gain in Equation 2.5 and consider the other terms. The rate of transitions is given by the well-known Fermi Golden Rule [10]
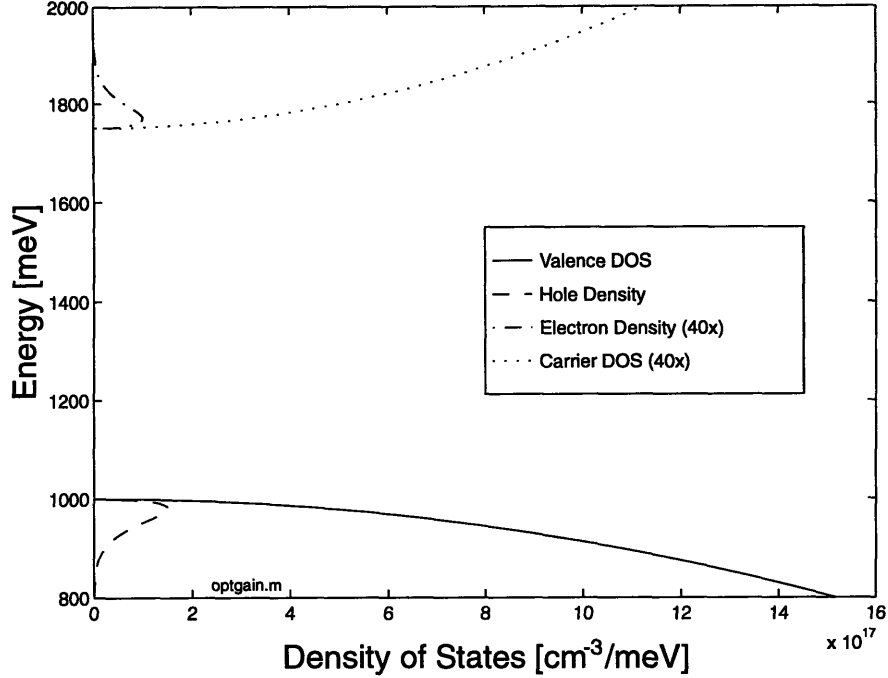
Figure 2.1   The density of states in both the conduction and valence bands plotted for various energies. Inset are the carrier and hole densities calculated with the appropriate Fermi distributions. Because of the difference in effective masses, the carrier densities are scaled by a factor of 40.

$$\gamma = \frac{q^2 h}{2 m^2 \varepsilon_0 n^2 E_{21}} |M|^2 , \tag{2.21}$$

where q is the electron charge, ε_0 is the permittivity of free space, and $|M|^2$ is the momentum matrix element. Since we have avoided full quantum mechanical calculations, the momentum matrix element may be approximated from the effective mass expression of $\mathbf{k} \cdot \mathbf{p}$ theory as [16, 17]

$$|M|^2 = \frac{m E_g}{4}\left(\frac{1}{m_c}+\frac{1}{m_v}\right). \tag{2.22}$$

Returning to Equation 2.5 of the gain, now we must integrate over all energy levels in the two bands separated by the energy E [18]:

$$g(E) = \frac{q^2 h}{2\varepsilon_0 m_c m_v cnE} |M|^2 \int_{-\infty}^{\infty} \rho_v(E_1)\rho_c(E_1 + E)(f_c(E_1 + E) - f_v(E_1))dE_1 , \tag{2.23}$$

where each energy, E_1, in the valence band is overlapped with the state in the conduction band separated by E. As with the simple rate equation expression, gain will occur when $f_c > f_v$, and no gain will occur when $E < E_g$ because the photon energy is insufficient to jump the band gap. Figure 2.2 shows the gain curve calculated using the parameters for a InGaAsP laser diode. In the calculation, the car-
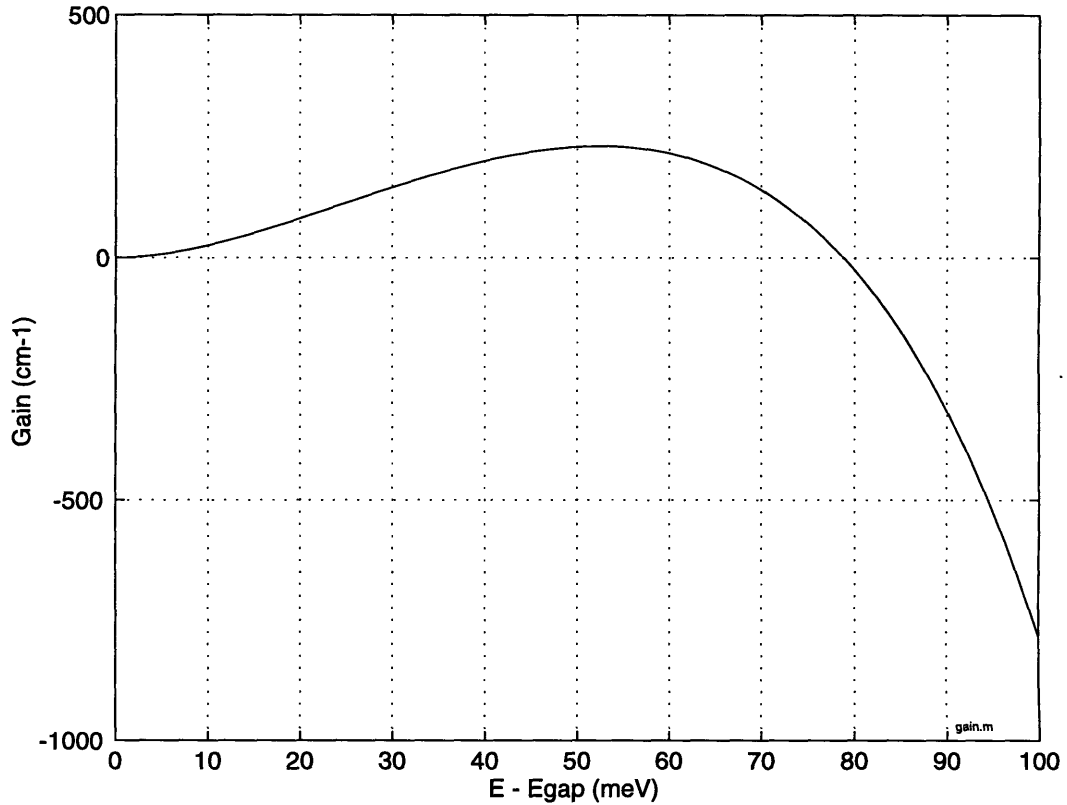
Figure 2.2   The gain coefficient calculated as a function of energy above the bandgap for an InGaAsP bulk diode laser with carrier density of 1.8×10^{18} cm^{-3}.

rier density was assumed and Equation 2.19 was solved numerically for the quasi-Fermi level for the electrons. Using charge neutrality in the device, the quasi-Fermi level for the holes was calculated similarly from Equation 2.20. Using these results, the gain curve could be calculated using the constants given in Table 1.

The gain curve is plotted versus the energy minus the band gap energy because below the band gap energy, the semiconductor is transparent. Gain will occur for energies between the band gap and the transparency point, where the gain passes through zero. The Bernard-Duraffourg condition sets the transparency point as the energy difference between the calculated quasi-Fermi levels for the two bands, $\mu_c - \mu_v$ [10]. Beyond transparency, the gain curve shows absorption, or net loss.

To determine how changes in gain affect the index of refraction, we must consider the susceptibility, which relates the electric field, $\mathbf{E}$, to the polarization, $\mathbf{P}$

$$\mathbf{P} = \varepsilon_0 \chi \mathbf{E}, \tag{2.24}$$

where χ is the susceptibility. The susceptibility has real and imaginary parts

Table 1: Values of constants used in calculation of gain coefficient.

Constant	Value
$\hbar$	6.6×10^{-13} meV·s
q	1.6×10^{-19} C
ε_0	8.8×10^{-17} $\dfrac{C}{mV \cdot cm}$
k_B	8.617×10^{-2} $\dfrac{meV}{K}$
T	300 K
n	3.6
E_g	750 meV
m_0	5.7×10^{-13} $\dfrac{meV \cdot s^2}{cm^2}$
m_e	$0.041 \; m_0$
m_v	$0.63 \; m_0$
c	3.0×10^{10} $\dfrac{cm}{s}$
N	1.8×10^{18} cm^{-3}

$$\chi = \chi_R - j\chi_I,$$
(2.25)

and may be written in terms of index and gain in the expression

$$\sqrt{1+\chi} = n - j\left(\frac{\lambda g_0}{4\pi}\right),$$
(2.26)

where n in the refractive index, λ is the wavelength, and g_0 is the linear gain. In this form, the Kramers-Kronig transformation [11, 12] defines the relation between the gain and index

$$n(\omega) = 1 + \frac{c}{\pi}\int_0^\infty \frac{g_0(\omega')}{\omega'^2 - \omega^2} d\omega'.$$
(2.27)

The integral may be rewritten in differential form to study the effect of changes in the gain on the index

$$\Delta n(\omega) = \frac{c}{\pi}\int_0^\infty \frac{\Delta g_0(\omega')}{\omega'^2 - \omega^2} d\omega',$$
(2.28)

which has been used in a number of theoretical and experimental studies [13, 14, 15].

Now we have a simple model for gain and index changes in a semiconductor diode laser. The density of carriers in the two bands governs the gain. Our model will allow us to see how changes in temperature and density create changes in gain. Then employing the Kramers-Kronig transformation the effect on the index can be determined.

2.2   Ultrafast Response of Semiconductors

The simple relations outlined in the last section enable us to interpret the response of the medium to both carrier density and temperature changes, and we will essentially reduce the study of ultrafast processes to the effects they have on the temperature and density distribution. In this framework we rely on experimental evidence for the identification of various ultrafast processes and then relate those changes to temperature and density changes in the distributions.

From the expressions for gain and density distributions, as the density of either carriers or holes changes, the quasi-Fermi levels will change. In these devices, the easiest means of increasing carrier density in the steady state is through current injection, and it is simple to perform experimentally. As the carrier density increases, a larger number of carrier states higher into the band are filled, resulting in a higher quasi-Fermi level. Similarly by charge neutrality, the hole quasi-Fermi level will drop, so the transparency point, as the difference between the two quasi-Fermi levels, will shift to higher energy. Figure 2.3 shows the gain curve for a variety of carrier densities, and as predicted, the transparency point shifts to higher energy with higher density.

Similar calculations may be done for changes in the temperature of the carriers, and the result is quite similar as Figure 2.4 shows. In this case, since the Fermi distributions are a function of temperature, changes in temperature alter the quasi-Fermi levels in the two bands. However, the relation between the quasi-Fermi levels and the temperature is inverse in the argument of the exponential; as the temperature increases, the quasi-Fermi separation decreases. Since the effective mass of the holes is higher than the electrons, a change in temperature of the holes will create a smaller change in the gain than a change in temperature of the electrons. Physically, the effective mass is inversely proportional to the curvature of the band in k-space, so the higher mass of the holes means the valence band is distributed over wide range of k-space and a narrow range of energy. Analogously, in the conduction band, the lower mass implies that the electrons are distributed over a narrow range of k-space and a wide range of energy. As the temperature is increased, because a large number of states are available in the valence band only a small change in gain is produced. On the other hand because only a narrow region of k-space can be filled in the conduction band, an increase in temperature creates a large change in available states for gain. In Figure 2.4 the temperature of both electrons and holes is kept equal.

The results we discuss above apply to gradual density and temperature changes, but they can also apply to much shorter time scales for a variety of phenomena. Here we consider several different phenomena which have been identified experimentally from pump-probe and other time-resolved measurements. Generally measurements of gain and index have been made, and changes with different time constants have been attributed to various physical processes which have been predicted to occur.

Stimulated absorption and emission create carrier population changes, which we initially considered with rate equations, recover via absorption or spontaneous emission with the carrier lifetime on a nanosecond time scale. In our experiments we typically only measure over 10 ps, so a process with such a long decay constant is indistinguishable from a step change. Auger recombination has also been observed at high densities with a time constant of 300-400 ps [19, 20]. Again these time constants are likely too large to be observed on the time scales of our experiments.

Spatial hole burning can occur in two forms. In the longitudinal case, if the facets of the amplifier produce significant reflections, then longitudinal standing waves can form. This creates alternating regions of high and low intensity via interference along the waveguide. Spatially, these regions will form with a period of half a wavelength, so the separation between regions of high and
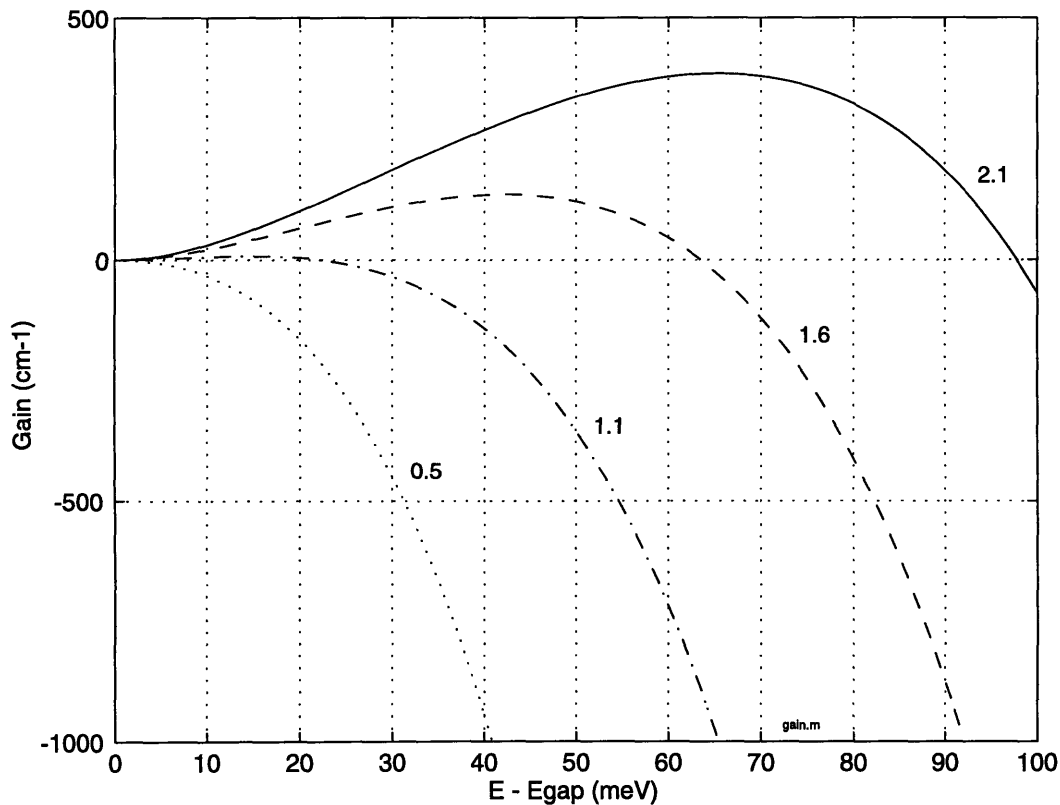

Figure 2.3   The gain coefficient calculated as a function of energy above the bandgap for the various carrier densities ($\times 10^{18}$ cm^{-3}) with all other parameters held constant.
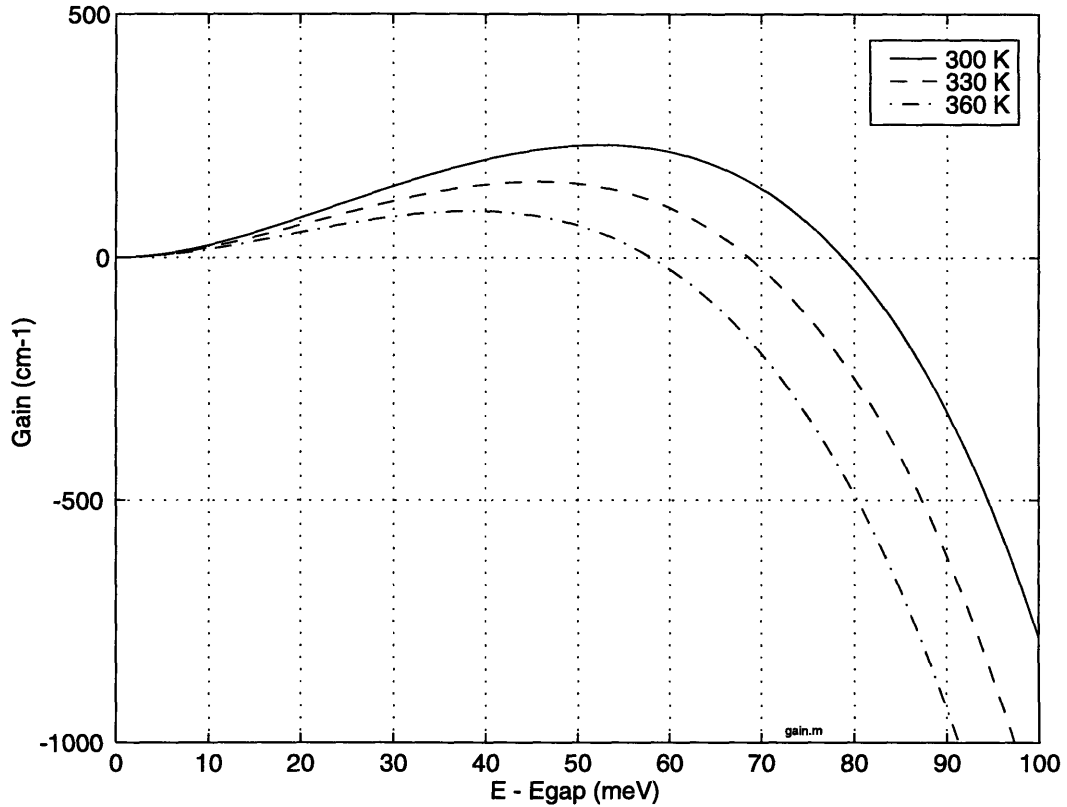
Figure 2.4   The gain coefficient calculated as a function of energy above the bandgap for several carrier and hole temperatures as indicated with all other parameters held constant.

low intensity will be on the order of 200 nm assuming 1.6 μm wavelength light and a waveguide index of 4. With such small spatial separation, the time for the grating to fill-in via diffusion is on the order of picosecond and could be calculated from semiconductor transport equations. However, in our case, with both facets AR-coated we assume that no significant standing wave patterns form.

Transverse spatial hole burning occurs when carriers from the cladding are not depleted or excited by the optical mode. Current leaking from the active region pumps the cladding layers of the amplifier. As the optical mode in the active region depletes carriers, carriers in the cladding region will move transversely to fill in depletion regions. As opposed to the longitudinal case, the distance the carrier must travel from the cladding to the active region is quite long and is a function of the confinement factor and cladding thickness. The carrier density gradients extend distances on the order of 1 μm, and the gain recovery time has been measured to be on the order of 100 ps [21]. Still this time is longer than the time scales we measure here.

The processes most significant in these experiments are those intrinsic properties of the semiconductor material. Two photon absorption (TPA) occurs when the energy of two photons is combined to stimulate a transition between the two levels. TPA is nonlinear, so a strong pump pulse could pro-

duce TPA with itself, but only a photon from the pump pulse combined with a photon provided by the probe pulse produces TPA that changes probe transmission. Since we perform pump-probe experiments in a small-signal regime TPA is observed during the time that the pump and probe pulse are overlapped, and it will always follow the intensity autocorrelation (assuming transform-limited pulses). Because the energy of two photons is taken, TPA can occur below band; in fact, it becomes the dominant process in below-band measurements. However, even when the energy of a single pump photon is sufficient to bridge the band gap, TPA will continue to occur. It is relatively wavelength independent [22, 23].

The recovery from spectral hole-burning occurs on time scales which experiments barely resolve. Since in our pump-probe experiments, the transitions are wavelength dependent and the spectrum of the pulse makes up only a small portion of the gain curve, transitions will reduce the number of carriers or holes in a limited energy range, creating a spectral "hole" in the conduction or valence band. The resulting non-Fermi distribution will eventually recover to a Fermi distribution via hole fill-in through carrier-carrier scattering. This time constant of hole fill-in is thought to be less than 100 fs [24, 25, 26, 27]. By inspection of the gain curve at transparency, we note that for the symmetric spectral width of a pulse centered at transparency a spectral hole cannot be formed because stimulated emission and stimulated absorption are equally probable,. The effects essentially balance, so it is an ideal point to eliminate spectral hole-burning from measurements.

Free carrier absorption (FCA) occurs when carriers in the conduction band instantaneously absorb a photon and are elevated to a higher lying state. Although typically not many conduction band electrons will be elevated in this way, the energy increase is quite large compared to other processes. For stimulated transitions most of the photon energy is used to cross the band gap, and the change in temperature of the electron or hole distribution is governed by how far above or below the average carrier energy the emitted or absorbed photon is. On the other hand with FCA, most of the energy of the photon will contribute to the carrier temperature. Although FCA may be significantly less likely than stimulated transitions, the effect on temperature is much greater.

TPA, FCA, and stimulated transitions all instantaneously move carriers in the two distributions. Immediately after these processes, carriers may be in a variety of unstable higher or lower energy states, but not in a Fermi distribution. Eventually these carriers will collide and quickly reestablish a Fermi distribution. As many of these carriers will still have a high energy, the temperature of the resulting Fermi distribution will be elevated, so these instantaneous processes create carrier heating. The time constant of carrier-carrier scattering required for the Fermi distribution to form is called the delay in carrier heating. Since carrier-carrier scattering is the physical explanation for this delay, it can be expected to have the same time constant as spectral hole burning. The elevated Fermi temperature will then slowly cool as carriers emit phonons, losing energy. The carrier heating recovery time constants have been measured between 600-1100 fs for devices similar to those we study here [1, 2, 4, 28, 29, 30].

Recently, some authors have suggested that heating recovery times may be lengthened via scattering to indirect valleys in the band structure [31]. Although this has not been identified in previous studies of structures similar to those we study here, it may exist and should be considered. However verifying that indirect transitions are affecting the carrier dynamics would likely require experiments with a variety of pump wavelengths.

2.3   Heterodyne Pump-Probe Theory

In a pump-probe experiment, we seek to measure the response of the semiconductor medium to a pump pulse passing through it by measuring the transmission of a probe pulse following it [5]. Here we consider the particular case of heterodyne detection, where pump is mechanically chopped for lock-in detection, and the probe and reference are generated with acousto-optic modulators (AOMs) which slightly upshift the frequency of the light [36]. Since all three signals are derived from the same laser pulse, we may represent them as

$$E_p = Re\left[E(t+\tau)c(t)e^{j\omega(t+\tau)}\right] \tag{2.29}$$

$$E_s = Re\left[aE(t)e^{j(\omega-\omega_1)t}\right] \tag{2.30}$$

$$E_r = Re\left[bE(t)e^{j(\omega-\omega_2)t}\right], \tag{2.31}$$

where E_p is the electric field of the pump, $E(t)$ is a complex amplitude, τ is the time delay between pump and probe pulses, $c(t)$ is the chopping function of the pump, ω is the optical frequency, E_s is the electric fiend of the probe, a is the complex amplitude of the probe, ω_1 is the frequency shift added by an AOM to the probe, E_r is the electric field of the reference, b is the complex amplitude of the reference, and ω_2 is the frequency shift added by an AOM to the reference.

As we will describe in the Chapter 3, in this particular heterodyne configuration the pump and probe pulses pass through the semiconductor optical amplifier (SOA), while the reference pulse passes around it. However, since the path length of the reference is adjusted to exactly match the probe, no linear phase difference is present between the reference and the pump and probe pulses, so we will neglect such a difference in this analysis. With this in mind, the electric field input to the SOA is

$$E_{in} = E_p + E_s. \tag{2.32}$$

Fields present in a nonlinear media will produce a nonlinear change in the material polarization, P, according to

$$\Delta P_i = \iiint dt'\, dt''\, dt'''\, \chi_{ijkl}^{(3)}(t-t',t-t'',t-t''')E_j(t')E_k^*(t'')E_l(t''') \tag{2.33}$$

where t', t'', t''' are all integration variables and $\chi_{ijkl}^{(3)}$ is the third-order nonlinear susceptibility generating a polarization P_i, from fields E_j, E_k, and E_l exciting the material with polarizations j, k, and l. Considering the properties of the nonlinear susceptibility, and can write the time derivative of the nonlinear polarization as

$$\frac{\partial \Delta P_i}{\partial t} = \int dt'' \, E_j(t) h_{ijkl}(t - t'') E_k^*(t'') E_l(t''),$$

(2.34)

where h_{ijkl} is tensor impulse response of the material that is related to the third-order nonlinear susceptibility.

This change in the material polarization will modulate the pump and probe fields. The output from the diode will then be the sum of a background signal, which is the linear transmission of the two incident fields with phase accumulation plus the added fields generated by the nonlinear polarization integrated through the distance of the active region. In heterodyne detection the output pump and probe fields from the diode will combine with the reference field in the detection fiber. Integrating over time for the response of a slow detector gives detected intensity as a function of the time delay

$$\Delta I(\tau) = \int dt |E_{out} + E_r|^2,$$

(2.35)

where E_{out} contains the changes in the pump and probe fields according to Equation 2.34. In calculating the change in intensity a large number of cross terms will appear, but because a heterodyne technique is used in conjunction with the mechanical chopping of the pump, most of the terms can be eliminated. Only terms with the reference and a single non-conjugated probe beam produce a beat signal at the heterodyne detection frequency of $\omega_1 - \omega_2$. Additionally, since lock-in detection is used by mechanically chopping the pump beam, only terms with the pump present as well are detected. With these two constraints the modulation of current on the detector, neglecting the spatial integration, is

$$\Delta I(\tau) = \int dt \, E_r^*(t) E_s(t) \int dt' \, h_{xxxx}(t - t') E_p^*(t' + \tau) E_p(t' + \tau)$$

(2.36)

$$+ \int dt \, E_r^*(t) E_p(t + \tau) \int dt' \, h_{xxxx}(t - t') E_p^*(t' + \tau) E_s(t') + c.c.,$$

(2.37)

where the impulse response has been written explicitly for the copolarized case and all beams are polarized in the x direction with respect to the nonlinearity. The first integral is the nonlinear response of the medium to the pump excitation, and the second integral is the coherent artifact produced by the overlap of the pump and probe pulses [5, 32, 33].

Since both detected integrals contain fields derived from the same source, they are proportional to a single electric field. The integral of Equation 2.36 may be written in a more useful form with a change of variable where

$$t - t' = \tau - t_1 \tag{2.38}$$

$$dt' = dt_1, \tag{2.39}$$

leaves the integral

$$I_{sig}(\tau) \propto \int dt_1 h_{xxxx}(\tau - t_1) \int dt |E(t)|^2 |E(t + t_1)|^2. \tag{2.40}$$

Since the inner integral is simply the intensity autocorrelation function, $G^{(2)}(t)$, the signal integral is

$$I_{sig}(\tau) \propto \int dt \, h_{xxxx}(\tau - t) G^{(2)}(t). \tag{2.41}$$

The coherent component may also be written in a similar form

$$I_{coh}(\tau) \propto \int dt \, E^*(t) E(t + \tau) \int dt' \, h_{xxxx}(t - t') E^*(t' + \tau) E(t'). \tag{2.42}$$

By inspection of the second integral, the coherent artifact is non-zero only when the pump and probe pulses are overlapped in the diode. Physically, for the copolarized case, as pump and probe pulses overlap they form a grating through interference, which can than scatter light into the pump or probe pulse measured at the output. From these expressions for copolarized beams, at zero time delay the two components are equal, so the coherent artifact must be considered for a proper understanding of data near zero time delay. Accordingly, in the past many authors removed the coherent artifact by subtracting half of the pump-probe response at zero delay. However, recently because of the identification of the spectral artifact, which will be outlined in the next section, this technique may not be appropriate [36].

In the cross-polarized case, where the pump is y-polarized and the probe and reference are x-polarized with respect to the nonlinearity, an artifact may or may not be present depending on the magnitude of the coupling in the third-order susceptibility tensor. For the cross-polarized case, following the same steps as the copolarized case, we obtain

$$I_{sig}(\tau) \propto \int dt \, h_{xxyy}(\tau - t) G^{(2)}(t) \tag{2.43}$$

$$I_{coh}(\tau) \propto \int dt \, E^*(t) E(t + \tau) \int dt' \, h_{xyyx}(t - t') E^*(t' + \tau) E(t'), \tag{2.44}$$

which are different from Equations 2.41 and 2.42 only in the tensor element selected.

In the cross-polarized case, instead of forming an intensity grating, the pump and probe form a polarization grating. The total field polarization changes as a function of delay, which preferentially excites orientation in the material. When the polarization reorientation time is faster than the optical pulsewidth, then the coherent artifact is zero. In semiconductors the polarization reorientation time is assumed to be less than 10 fs [22]. However, because TPA and other processes are assumed to occur

on that time scale, those portions of the ultrafast response may generate a coherent artifact [34], so in the cross polarized data presented here we assume the coherent artifact to be part of the instantaneous component.

In either the cross or copolarized cases, we detect the signals in the same manner. Through heterodyne AM demodulation and lock-in detection, the AM-demodulated signal is equal to the change in probe transmission

$$S_{AM}(\tau) = \Delta T(\tau),$$ (2.45)

and similarly for FM demodulation and lock-in detection, FM demodulated signal is the change in probe phase

$$S_{FM}(\tau) = \Delta \varphi(\tau).$$ (2.46)

The phase signal is related to the change in index of the material through the relation

$$\Delta \varphi(\tau) = \frac{2\pi L}{\lambda} \Delta n(\tau),$$ (2.47)

where $\Delta n(\tau)$ is the change in the refractive index.

2.4   The Spectral Artifact and System Response

In addition to coherent artifact, a spectral artifact has also been identified in pump-probe measurements [35, 36, 37, 38, 39]. Before this artifact was identified, data had been fit artificially with a phenomenological model which included two time constants which would combine to produce derivative effects [30, 27]. Now that a clear theoretical basis for the spectral artifact has been developed, it may be investigated experimentally. This artifact is a result of operating on a gain slope. Considering Figure 2.2, a spectrum of 100 nm centered at 1550 nm corresponds to a change in energy of approximately 50 meV, so a 100 fs pulse with even one quarter of that spectrum would cover a significant energy range. Except in the case where the spectrum would be centered at the top of the gain curve, a pulse spectrum will remain on a gain slope. In a sample which demonstrates both transmission and phase changes, a spectral artifact will be produced when the spectrum is on a gain slope. As we showed earlier, a nonlinear phase shift induced by the pump on the probe will create an index change, causing an shift in the frequency of the pulse. Because the pulse is effectively on a gain filter, the frequency shift is translated to an amplitude shift. Similarly an instantaneous amplitude change brings about a phase change, but typically it is a much smaller effect.

A mathematical form for this effect has been derived in detail by Mørk and Mecozzi for a variety of cases [36, 37]. In terms of the response functions theorized in previous sections related to the third-order susceptibility we can define a total response function

$$H(t) = \left(c_1 + ic_2 \frac{\partial}{\partial t}\right) h(t) \tag{2.48}$$

where H is the total waveguide response with the spectral artifact, c_1 and c_2 are both constants, and h contains both the real and imaginary parts of the material response defined as

$$h(t) = h_R(t) + ih_I(t), \tag{2.49}$$

where h_R is the real part and h_I is the imaginary part. Both responses have the same form, but different constants, so they may be written

$$h_R(t) = a_1\delta(t) + \left((a_2 + a_3)e^{-t/\tau_{SHB}} + a_3 e^{-t/\tau_{CH}} + a_4\right)u(t) \tag{2.50}$$

$$h_I(t) = \alpha_{TPA}a_1\delta(t) + \left((\alpha_{SHB}a_2 + \alpha_{CH}a_3)e^{-t/\tau_{SHB}} + \alpha_{CH}a_3 e^{-t/\tau_{CH}} + \alpha_N a_4\right)u(t), \tag{2.51}$$

where δ is the Dirac delta function representing processes much faster than the time resolution of the experiment, a_i are linear coefficients, τ_{SHB} is the time constant for spectral hole burning recovery, τ_{CH} is the time constant of carrier heating recovery, $u(t)$ is the step function representing population density changes, α_N is the linewidth enhancement factor for carrier density changes, α_{TPA} is the effective linewidth enhancement factor for TPA, α_{SHB} is the effective linewidth enhancement factor for SHB, and α_{CH} is the effective linewidth enhancement factor for carrier heating. After substitution, the total response has the form

$$H(t) = c_1 h_R + c_2 \frac{\partial h_I}{\partial t} + i\left(c_1 h_I + c_2 \frac{\partial h_R}{\partial t}\right). \tag{2.52}$$

The real and imaginary parts of this response function can be used to fit experimental data if both transmission and phase data are available. The relative importance of the derivative of the phase on the amplitude and the derivative of the amplitude on the phase is determined by the magnitude and sign of the various linewidth enhancement factors. Although fitting appears quite difficult, it is possible with this function if both data sets are available and time-synchronized.

CHAPTER 3: EXPERIMENT DESIGN

The concept of a pump-probe experiment is relatively simple but implementation to obtain sub-picosecond resolution at the wavelength of interest can be very difficult. Here we consider opto-electronics devices used in the communications band near 1.55 μm. For these experiments a source with femtosecond transform-limited pulses, sufficiently high power, a high repetition rate, long term stability, low noise, and easy operation would be ideal. Until just recently there have been few laser sources capable of attaining all of these attributes.

Previously, Additive Pulse Modelocked (APM) F-Center lasers were virtually the only source capable of producing femtosecond pulses near 1.5 μm. We can understand the advantages and disadvantages of the recently developed fiber laser by considering such a competing source. The F-center laser is based on the KCl:Tl crystal pumped synchronously via an actively modelocked Nd:YAG laser. Short pulses are attained through an intensity dependent phase shift in an auxiliary fiber cavity [40]. When modelocked, the laser typically produces pulses with duration between 120-170 fs with an average power of 100 mW at a repetition rate of 100 MHz, yielding a pulse energy near one nanoJoule. Through APM action, the pulses are virtually chirp free with a time-bandwidth product between 1.1 and 1.3 times the transform limit. Clearly, when the color center laser works, it is an excellent source; but there are a number of obstacles to maintaining a color center. The crystals are quite sensitive to moisture, temperature, and light, so they must be kept at liquid nitrogen temperatures in vacuum dewars [41]. Since APM is essentially a result of optical interference, APM requires interferometric stability between two different cavities [42]. (Note that cavity stabilization is also a weakness of other Optical Parametric Oscillator (OPO) systems that are now available at 1.5 μm.) The maintenance and stabilization requirements of a color center laser, make it very difficult to perform systematic experiments, so experimentalists have eagerly awaited an alternative.

3.1   *The Erbium Doped Fiber Laser*

Developed for the fiber communications industry, glass fiber doped with various rare earth atoms, erbium in particular, has become commercially available. Researchers have investigated fiber lasers in a variety of forms, and modelocking has been attained in a number of configurations [43, 44]. One of the most versatile and robust fiber lasers is the stretched-pulse APM (SP-APM) erbium-doped fiber ring laser [45, 46, 47]. The particular fiber laser configuration used in these experiments is described in detail by G. Lenz, et al. [48].

Originally in this laser the erbium fiber was pumped by a continuous-wave Ti:Sapphire laser at 980 nm, but now high-power diode lasers are available at this wavelength. We use a Master Oscillator Power Amplifier (MOPA) available from Spectra Diode Labs (SDL) which supplies up to 1 W of 980 nm continuous wave power. The diode driver only requires a single standard AC outlet, instead of three-phase power and water cooling required of solid-state systems. The diode contains a single-lon-gitudinal-mode oscillator integrated with a power amplifier as well as bulk optics to produce a diffraction limited beam with an excellent spatial mode. We typically operate the MOPA at 75% of the maximum output power, or 750 mW, to preserve its operating lifetime. As a relatively new research product, the MOPA exhibits a number of idiosyncrasies and the lifetime is still questionable at best. However, when it operates well, it is an excellent source. We operate the diode driver typically at 200 mA for the oscillator, 2700 mA for the amplifier, and at a temperature of 25°.

As a semiconductor diode laser, the MOPA is quite sensitive to back reflections, so care must be taken in coupling its output to other optics. The output is coupled into an angle-polished fiber with two beam-walking mirrors through an aspheric lens mounted on an X-Y differential-micrometer stage. We have attempted coupling in a variety of configurations with specialized coupling lenses, telescopes, and aspherics combined with convex lenses, and have found single aspheric lenses with focal lengths between 7 and 14 mm provide the most consistent performance with coupling typically near 70%. The coupling can be measured with a silicon photodiode by using a 2% fiber coupler spliced to the input fiber. Again, to avoid backreflections all output fiber ends must be angle polished as well. We have observed that the percentage of coupling may vary with temperature and polarization state at the coupler, so the monitored power may not be an accurate measure of the power in the fiber but is still useful for optimizing coupling.

Once the laser is modelocked, it usually remains very stable for long periods of time. Although modelocking is typically self-starting, we allow the system to warm up for at least an hour before checking for modelocking because of thermal effects in the MOPA. We monitor modelocking on a fast InGaAs diode from the reflection of the front face of the birefringent tuning plate, which allows all the output power from the high-power port to be used for experiments. As Figure 3.1 shows, we measured the output power as a function of coupled pump power, using a silicon filter to eliminate
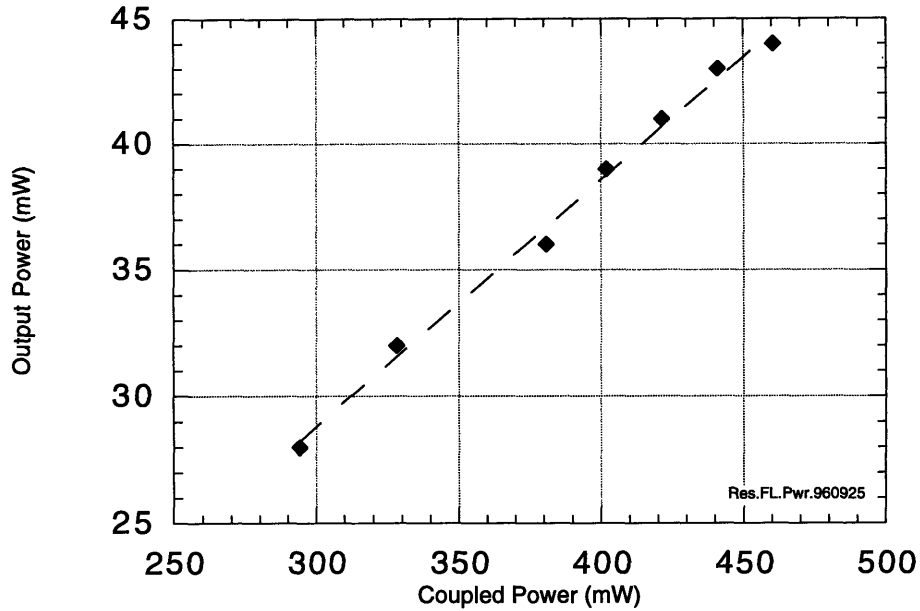
Figure 3.1   Modelocked power from the rejected output port of an erbium-doped stretched-pulse fiber ring laser. Measured with a silicon filter to eliminate any residual 980 nm pump light, and characterized as a function of coupled 980 nm pump power.

980 nm pump light. Our particular laser contains only 1.3 meters of erbium fiber, and other investigators have developed lasers with output powers near 100 mW using longer lengths of gain fiber [49].

We have obtained stable modelocking with two different polarization states set by waveplate combinations in the laser. However in one of the settings the laser produces satellite pulsing. The autocorrelation appears as a central pulse followed by a second pulse within 10-20 picoseconds, creating a pedestal structure. Although the fast detector will not indicate this satellite pulsing, the spectrum is clearly bimodal, so an optical spectrum analyzer will reveal the condition. Although these pulses are undesirable for spectroscopy, the laser is less sensitive to back reflections in this state. True symmetric double pulsing can also be obtained, but since the laser repetition rate is 39.55 MHz, the doubled period is 12.6 ns, which is easily distinguished on the fast detector.

In the other polarization state, the fiber laser rejected output has a very broad spectrum and very clean chirped pulses. As mentioned, in this setting the laser is quite sensitive to backreflections, so we had to add a 30 dB isolator immediately after the laser output to prevent backreflections from stalling the laser. Backreflections from a half-wave plate were sufficient at times to stall the laser when properly modelocked. However, insertion of the isolator eliminated this problem.

The output spectrum of the fiber laser with the optimized settings is shown on both linear and log scales in Figure 3.2. The spectrum is roughly 60 nm wide, but the log scale shows that some usable power is available over nearly 100 nm. The output pulses are highly chirped, but they are fitted quite well by a hyperbolic secant shape as shown in Figure 3.3. We attempted to pump-probe a diode with
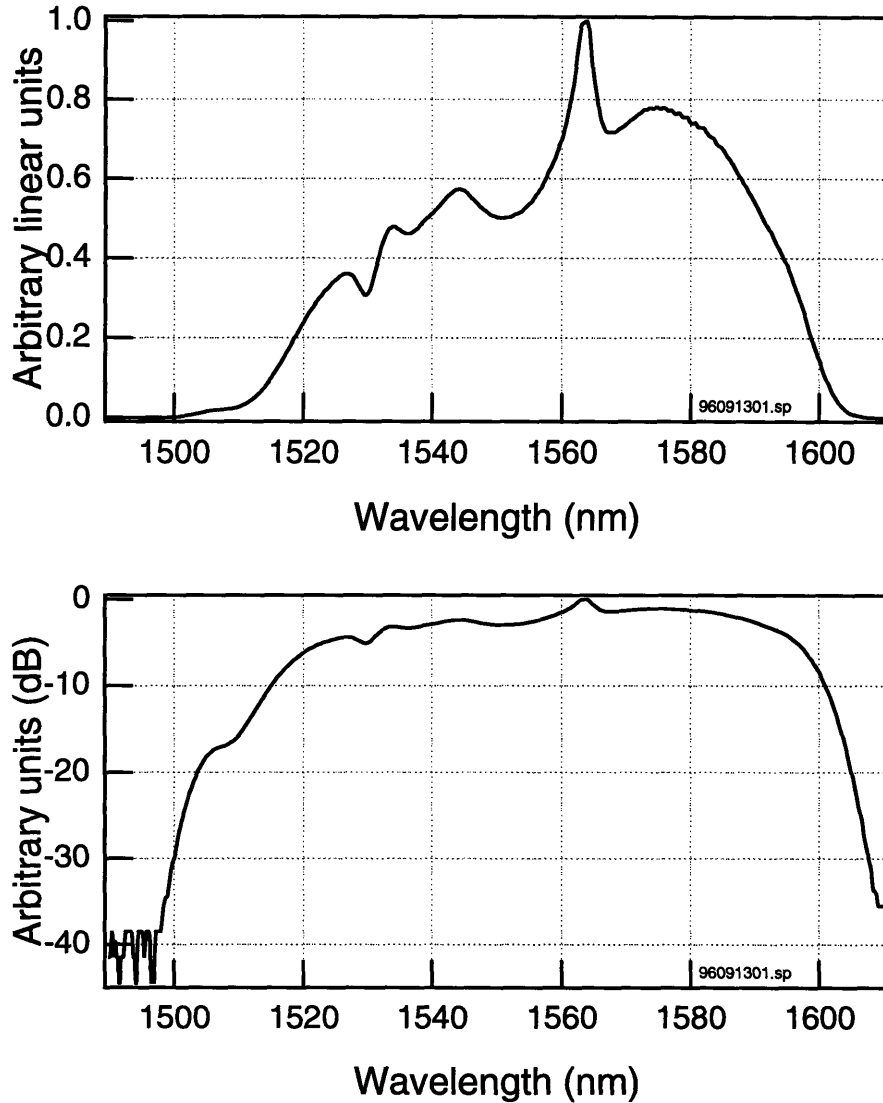
Figure 3.2   The spectrum directly from the rejection port of the modelocked fiber laser measured on an optical spectrum analyzer. Shown on both linear and logarithmic scales to highlight the breadth of the spectrum.

the pulses directly from the fiber laser, but the chirp was so severe that artificial time components were generated, making interpretation of the data virtually impossible. However, because the output spectrum is so large, compression is a logical option.

3.1.1   Pulse Compression

Others have reported compressing the pulses from the rejection port of the SP-APM laser to as short as 89 fs using four silicon prisms and an adjustable slit [48]. Here we have chosen to use two Brewster cut silicon prisms and a right angle prism in a double pass configuration [50]. Compression
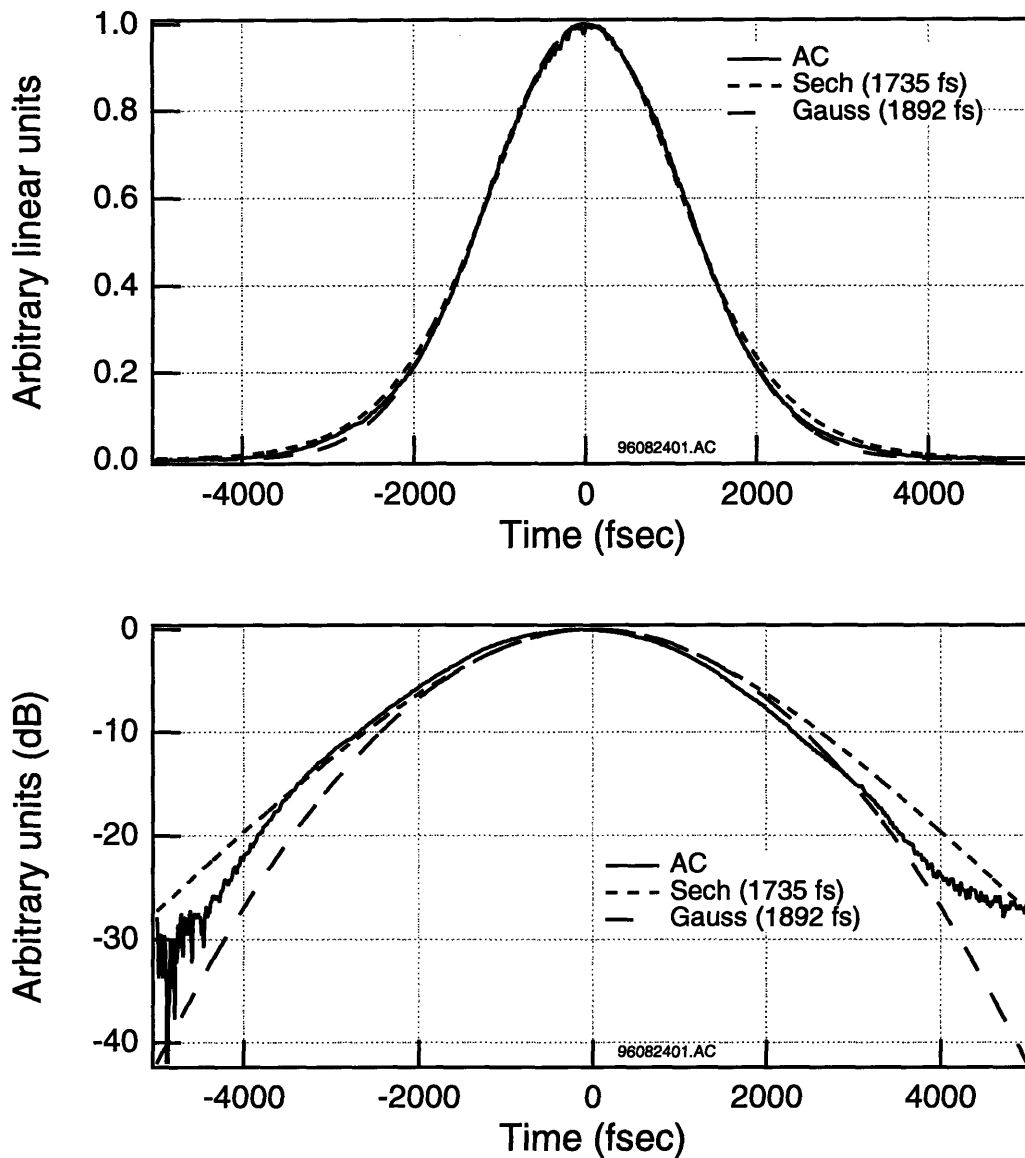
Figure 3.3   Autocorrelation of modelocked pulses directly from the rejection port of the fiber laser without compression. The hyperbolic secant and gaussian best fits are overlaid with pulse duration in parenthesis. The logarithmic scale is shown to resolve the wings of the pulse.

occurs after the rejection port output has passed through an 30 dB isolator to prevent backreflections, a half-wave plate because the rejection port output is S-polarized instead of the P-polarized admitted by the prisms, and beam steering optics as shown in Figure 3.8.

Prism alignment is a tedious task, but can be simplified somewhat with a few techniques. For the small half-inch prisms used here, beam clipping can be a serious problem, and should be constantly checked. The prisms are mounted on stages that provide translation in two directions, tilt in two directions, and rotation around one axis. We have found that all degrees of freedom are necessary for peak

alignment. Initially we align the prisms by finding the minimum angle of deviation as the beam passes through each prism at Brewster's angle. After checking minimum deviation through both prisms, the beam may be returned with a right angle prism, a mirror at an angle, or a retroreflector, the only requirement being that the beams be separated sufficiently to pick off the compressed beam. However, reflection in parallel but just below the input beam path appears to work best. To adjust the prisms we have found maximizing SHG to be the most repeatable method. Maximizing the SHG signal will favor shorter pulses, while remaining sensitive to clipping through the prisms. Although initial alignment often requires lock-in detection, a silicon detector may be used when signals have reached reasonable levels. When pulses are compressed, the SHG output is typically between 5-10 μW, enough to detect over ambient light. We have observed that maximizing SHG will lead to clipping at the second prism, which corresponds to spectral filtering. Although, power is lost in the clipping, the gain in pulse shortening is typically worth the loss.

The pulses obtained after compression are shown on linear and log scales in Figure 3.4. Although the fits indicate a short pulse-width, they fit only the central part of the pulse and a large portion of the pulse energy remains in the wings. Since the quality of a pump-probe trace will depend on the shape of the autocorrelation function, better pulses are needed. Although slight clipping occurs in the compression stage, the spectrum is essentially the same as in Figure 3.2, so the need for further spectral filtering is obvious to obtain transform-limited pulses.

3.1.2 Spectral Filtering

One way to determine if pulses are transform-limited is to compare an estimated time-bandwidth product based on full width half maximum (FWHM) values for the spectrum and autocorrelation. We calculate the time-bandwidth product from

$$\Delta\tau\Delta\nu = \Delta\tau\Delta\lambda\frac{nc}{\lambda_0^2} \tag{2.53}$$

where $\Delta\tau$ is the FWHM of the electric field for the assumed pulse shape, $\Delta\nu$ is the bandwidth of the pulse frequencies, $\Delta\lambda$ is the width of the spectrum, λ_0 is the center wavelength, and c is the speed of light. However, for pulses close to transform-limited, the FWHM of the electric field may be approximated by the FWHM of the autocorrelation. From the Fourier transform, the minimum time-bandwidth product for hyperbolic secant pulses is 0.314, so by comparing to this value we can estimate how close the pulses of the fiber laser are to transform-limited. Using the Δt from Figure 3.4 and the Δl from Figure 3.2, we obtain a time-bandwidth product that is 2.31-times transform-limited. In pump-probe experiment pulses under 1.5-times transform-limited are needed, so spectral filtering is in order.

Here we have used an interference filter for spectral filtering. An interference filter is made up of one or several dielectric stacks that will provide an almost fixed bandpass, with the center wave-
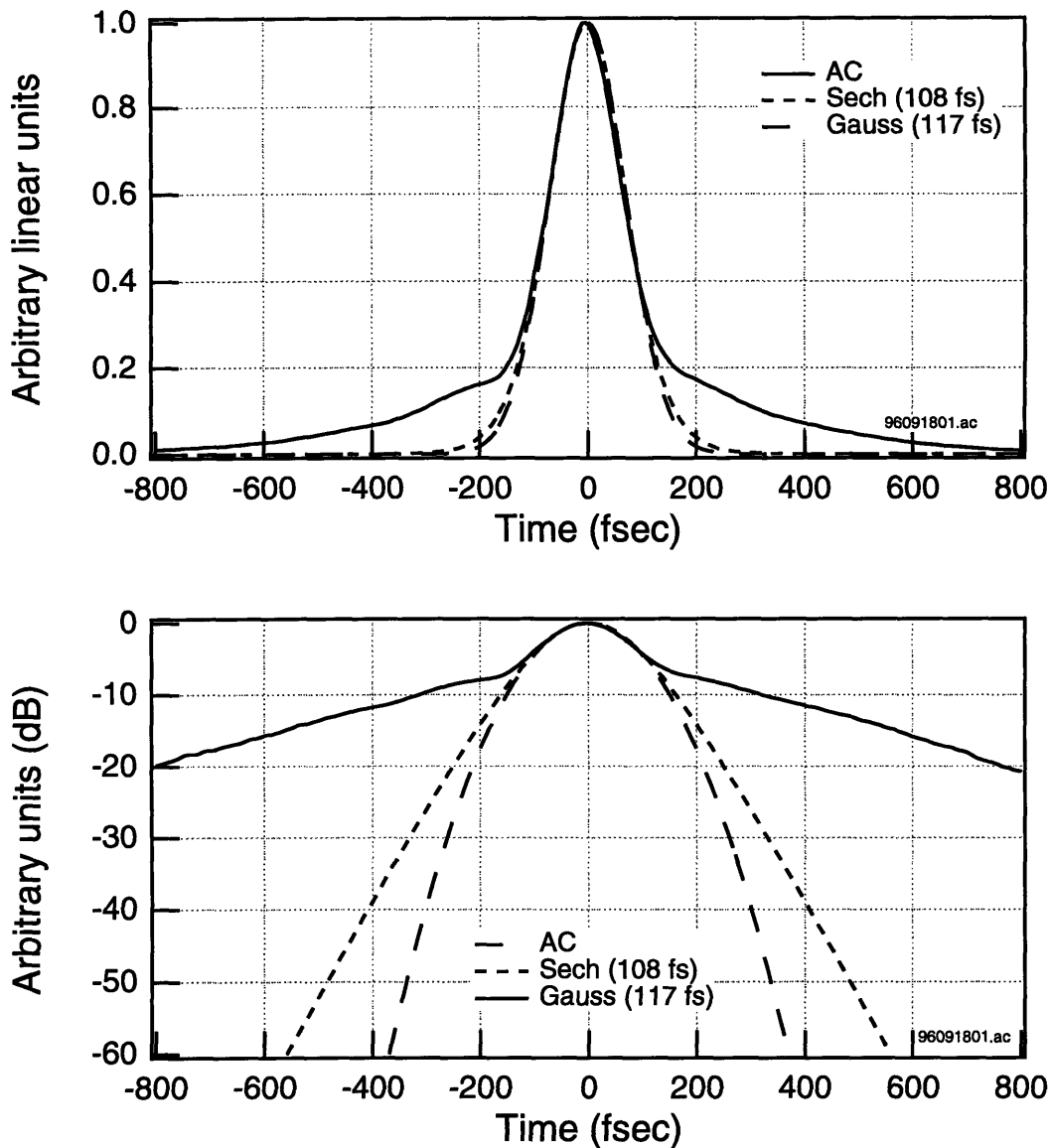
Figure 3.4   Autocorrelation of modelocked pulses from the rejection port of the fiber laser after compression through a double-pass silicon prism pair. The hyperbolic secant and gaussian best fits are overlaid with pulse duration in parenthesis. The logarithmic scale is shown to resolve the wings of the pulse.

length tunable as the filter is tilted or heated, to change the effective stack thickness. In selecting a bandpass, we calculated the $\Delta\lambda$ required for transform-limited 100 fs pulses and ordered a double cavity interference filter centered at 1600 nm at normal incidence with AR coatings on both sides to reduce losses. Via angle tuning, the center frequency can be tuned from 1600 nm at normal incidence to below 1500 nm at around 30°. The out-of-band rejection on such a filter is typically specified to be about OD 3-4, or 3-4 orders of magnitudes below the maximum. Transmission of the peak in the filter
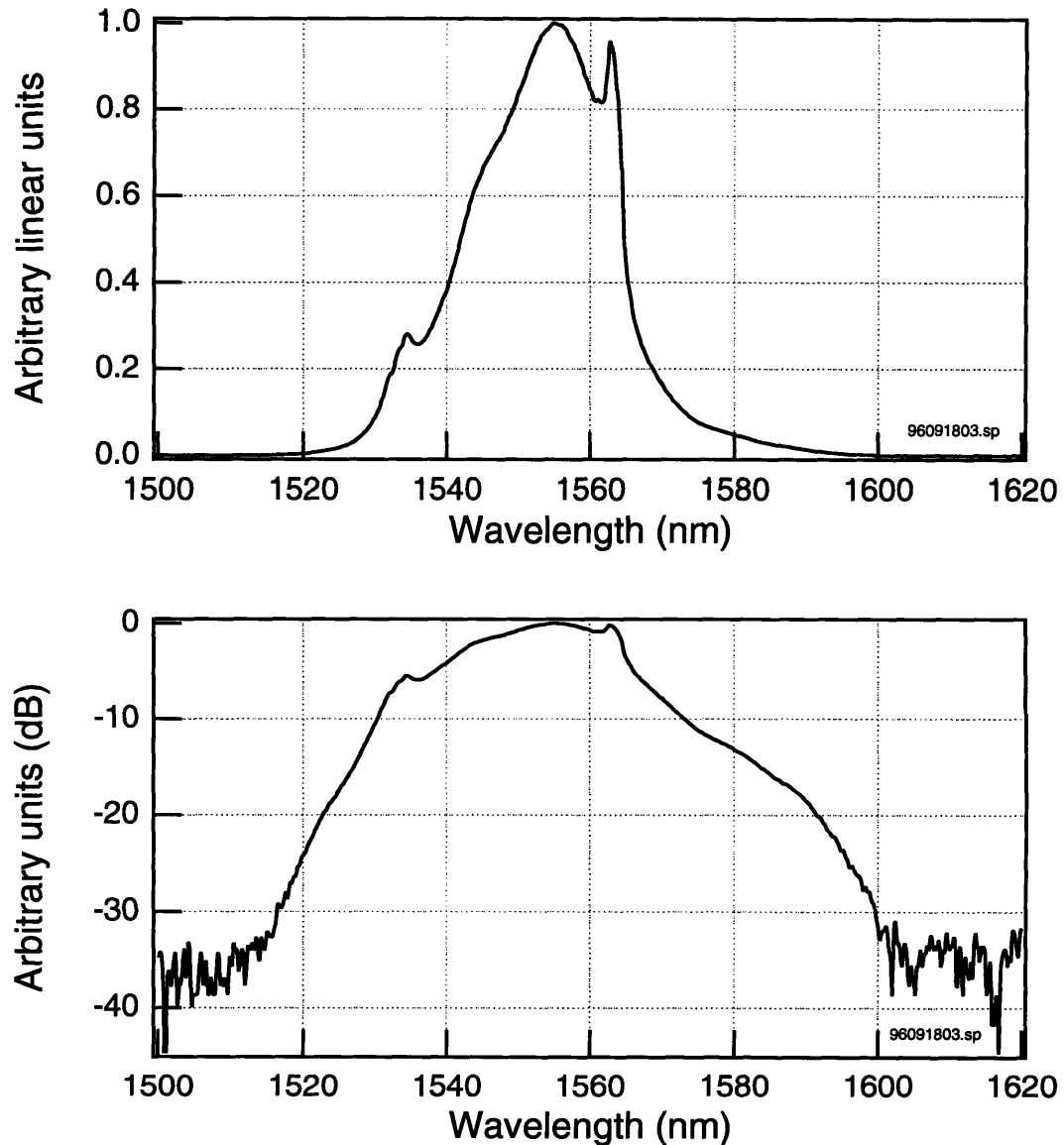
Figure 3.5   Modelocked fiber laser spectrum after spectral filtering of compressed pulses through an interference filter. The logarithmic scale is shown to evaluate the interference filter rejection across the full spectrum. The FWHM of the spectrum is approximately 23 nm.

is around 80-90%, and with the double cavity configuration, it essentially follows a hyperbolic secant shape.

We placed the filter following the compression stage and optimized the incident angle for the shortest pulses, this resulted in a spectral first moment for the transmitted light of 1553 nm. The spectrum and autocorrelation after the filter are shown on linear and log scales in Figures 3.5 and 3.6. Comparing the spectrum after the filter with that of the initial fiber laser output in Figure 3.2 shows that although the filter performs reasonably, characteristic spikes in the spectrum remain. From the
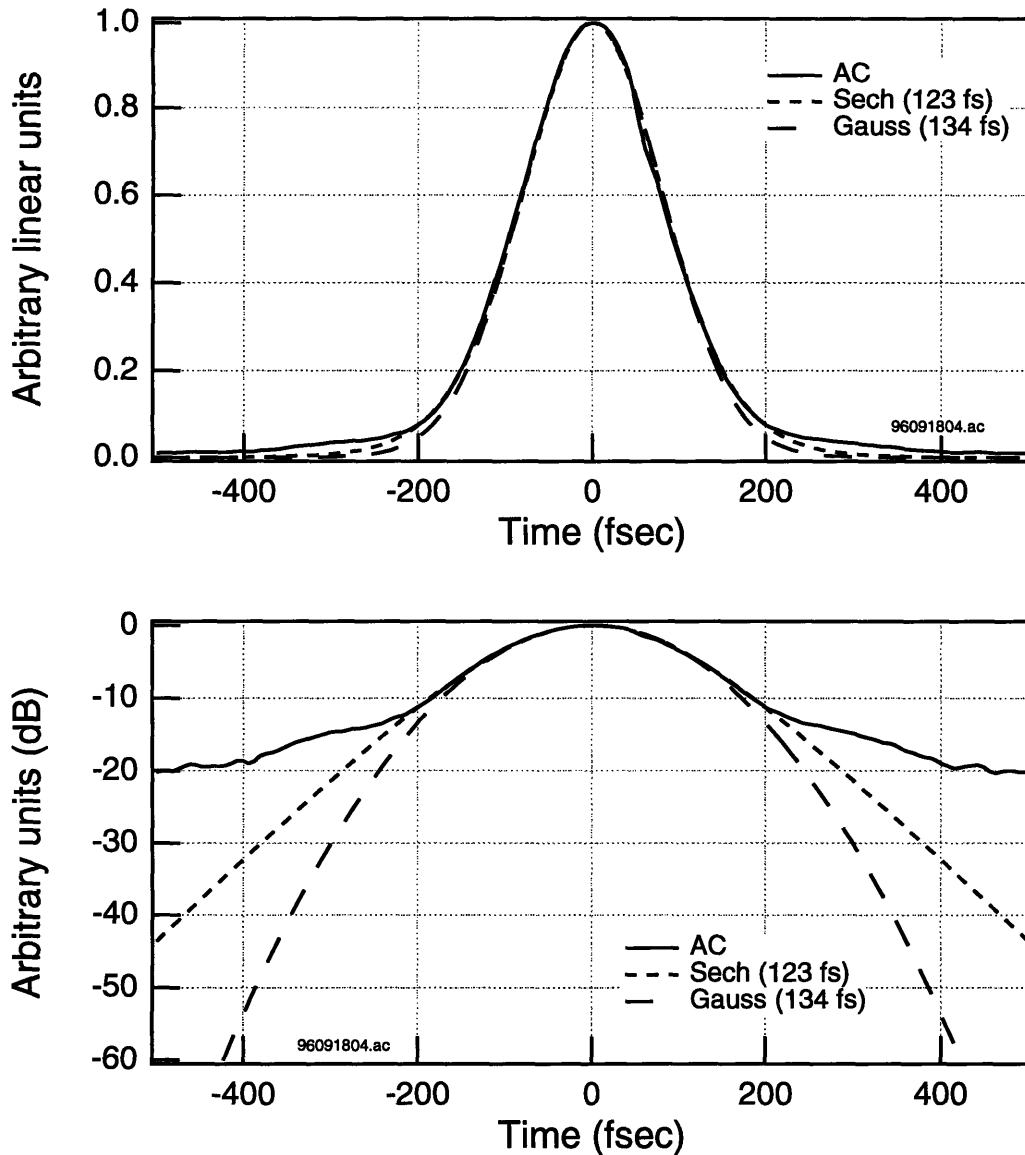
Figure 3.6   Autocorrelation of modelocked pulses from the rejection port of the fiber laser after compression and spectral filtering through a double-pass silicon prism pair and interference filter. The hyperbolic secant and gaussian best fits are overlaid with pulse duration in parenthesis. The logarithmic scale shows the pulse duration is longer than for unfiltered pulses, but the wings are significantly smaller.

spectrum and autocorrelation, $\Delta\tau = 123$ fs and $\Delta\lambda = 23$ nm, producing a time-bandwidth product that is 1.11-times transform-limited. Although on a day to day basis pulses are typically 130-140 fs, this still produces pulses that are under 1.3 times transform-limited, which is certainly sufficient for the pump-probe measurements we perform.
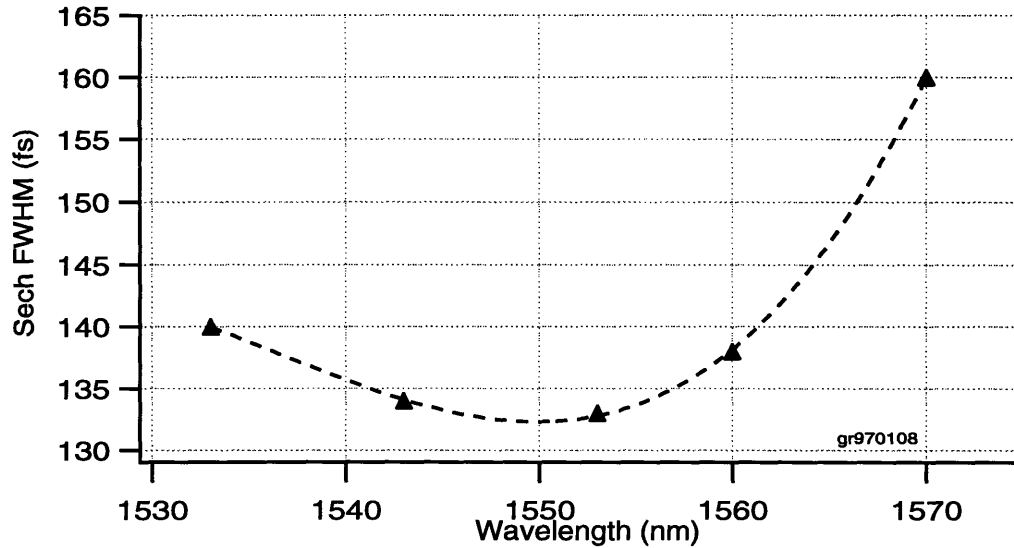
Figure 3.7   The pulsewidth attained by angle tuning an interference filter to select the center wavelength of the compressed spectrum without changing other parameters. At the two extreme wavelengths the pulses exhibited significant wings.

3.1.3   Wavelength Tunability

The interference filter provides the added benefit of wavelength tunability. Because only a small portion of the fiber laser spectrum is necessary to produce the desired pulses, it should be possible to tune significantly. To test this possibility, the filter was angle tuned across the range of the fiber laser spectrum, and an autocorrelation was taken at each point. A plot of pulsewidth versus center wavelength is shown in Figure 3.7. The only adjustment other than changing the angle of the filter was to steer the beam into the autocorrelator. The prisms had been set for the entire spectrum without consideration for the pulse width after the interference filter. Pulses of under 150 fs were obtained over a 35 nm range which is quite promising. At the far edges of tuning, the pulse shape was beginning to degrade with wings appearing. With angle tuning the bandwidth of the interference filter changes slightly, so this might be the source of part of the pulsewidth changes, but the majority of the variation is likely due to the shape of the original spectrum. Nevertheless, the plot demonstrates the possibility of independent tuning of pump and probe derived from the same source beam, which could be quite useful in some experiments.

Although angle tuning of wavelength seems possible from the width of the fiber laser spectrum, the tuning is limited by power and the shape of the spectrum. One method to eliminate these problems could be through the use of the non-rejected APM port of the fiber laser and then amplification with an erbium amplifier. Free space use of the non-rejected APM pulses has been demonstrated with nearly 15 mW of output power [51]. Because the spectrum is significantly better from this port,

slicing it may produce better pulses. To make up for the power loss, it could be sent through a simple erbium amplifier, and then compressed subsequently as it is currently. Then spectral filtering may produce useful power at an even broader range of wavelengths with shorter pulses.

3.1.4   The SP-APM Compared to Other Sources

Considering the results presented here, the fiber laser does seem to be an excellent alternative to other spectroscopic sources, specifically color center lasers. In terms of pulsewidth, the fiber laser can produce near-100 fs pulses easily, and sub-100 fs pulses in some cases. The repetition rate is approximately half that of a typical solid state laser system, but in terms of signal-to-noise, the factor of 2 is not so significant. On the other hand, compared to 1-250 kHz continuum-generation amplifier systems, the higher repetition rate is quite significant in reducing noise via averaging. Output power of the fiber laser is typically significantly lower than most solid state systems. However, for most pump-probe experiments on active waveguides, higher powers are not needed because it is desirable to stay within a perturbational regime in the device of interest. The tuning range of the fiber laser is comparable to a modelocked color center laser, but significantly less tunable than an OPO system [52], and certainly less tunable than continuum generation [53]. Cr:YAG has also recently been demonstrated as a source of very short tunable pulses near 1.5 μm [54], but to date it has not been demonstrated as a consistent spectroscopic tool. In terms of stability, the fiber laser is perhaps the most stable system available. Compared to an actively stabilized cavity, it is unquestionably better. Finally in terms of maintenance and ease of use, the fiber laser is perhaps easier to operate than any other passively mode-locked femtosecond laser available. For experiments that require systematic studies of several different samples at 1.5 μm it is perhaps the best source available for low excitation levels.

3.2   Heterodyne Pump-Probe

As outlined previously, a pump-probe experiment seeks to measure the response of a semiconductor by exciting it with a pump pulse and then observing the effect on the transmission and phase of a probe pulse. Typically, collinear pump-probe experiments are performed in a cross-polarized configuration where the pump and probe pulses are distinguished by polarization. Here we implement the more versatile heterodyne technique, which allows the pump and probe to be set at arbitrary polarizations, and has been used in a number of studies [55, 56, 57, 58].

Heterodyne pump-probe is accomplished by frequency shifting the probe and creating a reference that is also upshifted to interfere with the probe in detection. Experimentally this is accomplished with acousto-optic modulators (AOMs) in the system as shown in Figure 3.8. The beam from the fiber laser is passed through a flint glass AOM to generate the probe beam up-shifted 40 MHz. This AOM can introduce pulse broadening. It can be pre-compensated in the prism compression, although exper-
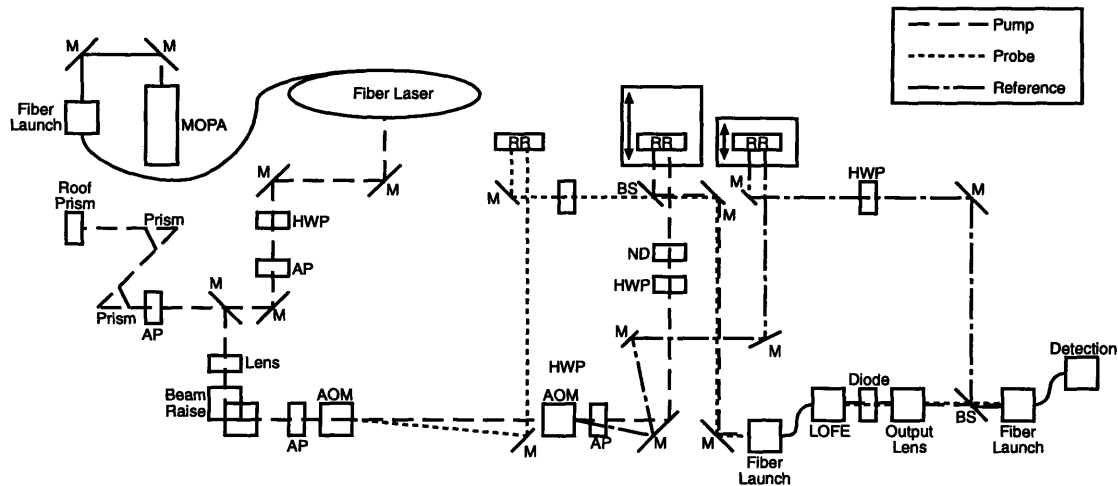
Figure 3.8   The complete experimental system for the heterodyne pump-probe experiment including the fiber laser and compression stage. M - gold mirror, HWP - zero-order half waveplate, AP - aperture, AOM - acousto-optic modulator, RR - retroreflector, BS - beam splitter, and ND - variable neutral density filter.

imentally the pulse broadening is virtually insignificant. The non-shifted signal is passed through a second, silica AOM to generate the reference beam up shifted by 39 MHz. The pump pulse reflects off a retroreflector mounted on a micro stepping stage to automate the time delay, and then is combined with the probe pulse at a beam splitter. The beams are then coupled into a fiber spliced to a Laser Optical Fiber Interface (LOFE), which is a fiber-coupled lens assembly designed for coupling into optical amplifiers. The length of fiber is made as short as possible to avoid polarization scrambling. At the output of the diode, a large-numerical-aperture aspheric lens is used for output coupling. In parallel, the reference beam travels around the device, reflects off a mirror mounted on a PZT transducer, and combines with the pump and probe beams from the device at a beam splitter. All three beams are coupled into a fiber, and detected on a detector tuned to 1 MHz beat, which the probe and reference beat to produce. The filtered signal is detected by a Ham radio receiver in either AM or FM mode which passes an amplified signal to a lock-in for final detection.

We use techniques to calibrate the system for amplitude and phase measurements. For amplitude measurements, the probe beam is mechanically chopped; and with the pump blocked, the 1 MHz signal is measured to determine the transmission without pump modulation. Calibration of the phase measurements is more complicated. An interferometer is constructed around the PZT in the reference arm, the two beams with relative delay are coupled into a fiber and the transmitted power is measured on a detector. By varying the PZT voltage, one can generate a sine curve as the reference beam interferes with itself, as shown in Figure 3.9. From this graph the voltage on the PZT required for a π phase shift can be determined. From the calibration data, the voltage for a π phase shift in the system is known, and the PZT can be fully modulated at that voltage, while the 1 MHz beat signal is detected. Then the lock-in voltage corresponding to a π phase shift is known.
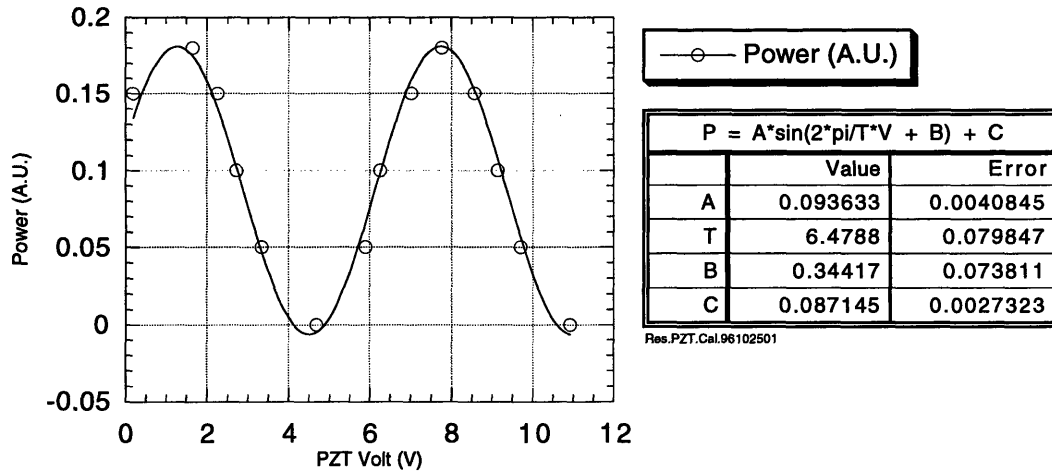
Figure 3.9   Calibration of the piezoelectric transducer (PZT) for the reference of the phase measurements. The full modulation depth indicates that a π phase shift has been attained. Since in this measurement the mirror mounted on the PZT was passed twice, one-quarter the period, T, of the fit provides the voltage required for such a π phase shift in the experiment.

CHAPTER 4: HETERODYNE PUMP-PROBE RESULTS

We used the experimental system outlined in the previous chapter to attempt to resolve the spectral artifact in pump-probe data. Obtaining phase and amplitude data simultaneously makes fitting for the spectral artifact possible. Initially we performed a diagnostic of the system by performing a bias-lead monitoring experiment. We performed full heterodyne pump-probe experiments on standard multiple quantum well (MQW) diode amplifiers. Initially we investigated the linearity of these amplifiers to insure all measurements were in a perturbational regime. Here we compares these pump-probe measurements qualitatively to results obtained previously on similar devices. Finally we attempt to resolve the importance of the spectral artifact component and discuss various fitting techniques appropriate for the data.

4.1   Bias-Lead Monitoring Diagnostic

As we designed the experimental system, we planned a simple test to ascertain whether the fiber laser would be an appropriate source. We implemented the bias-lead monitoring technique for ultrafast nonlinearity measurements [59]. The technique is quite simple because it uses the diode under investigation as a detector by measuring the diode junction voltage. Previously, the technique had been used on a bulk InGaAsP amplifier, but it is certainly applicable to the similar MQW device we consider here.

The technique is essentially a pump-probe experiment without the additional detection electronics after the optical amplifier. For this measurement, we use the experimental system shown in Figure 3.8. In the experiment only pump and probe beams are required since the full heterodyne technique is not used for the detection. This is accommodated quite easily because the AOMs in the experimental system provide an adjustable defracted power. In this case no power was transferred to the reference beam. In the experiment performed here, the pulses were compressed, but the spectral filtering technique was not used. The pulses exhibited relatively significant wings although the hyperbolic
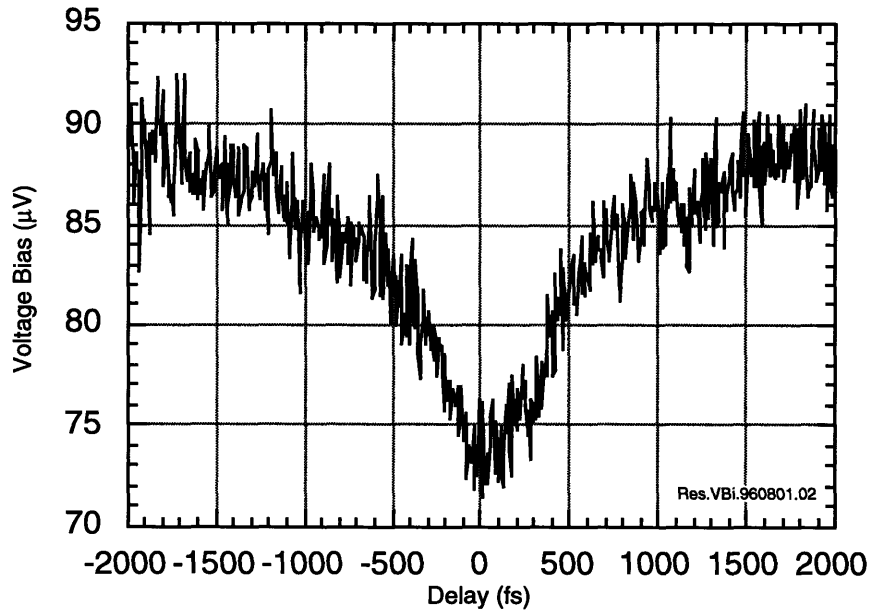
Figure 4.1   Bias-lead monitoring of a strained-layer MQW diode using 130 fs compressed but not spectrally filtered pulses. Note that the small change in the response is on top of a large signal offset, making the measurement difficult to resolve.

secant fit produced a FWHM of 130 fs. For the maximum signal, both pump and probe were at equal intensity with one of the beams chopped by a mechanical chopper to employ lock-in detection. The terminals across the current source connected to the diode were then connected to the voltage input of the lock-in amplifier. The high impedance of the lock-in input assured that it would not draw current while in parallel with the very low resistance of the diode.

The delay between the pump and probe beams was scanned with the mechanical stepping stage, and the voltage across the diode was measured with the lockin. Figure 4.1 shows the measured voltage as a function of pump-probe delay. The poor signal-to-noise ratio on the trace is because the entire signal sits on a large background signal. In this case, the signal change was approximately 20% with as much power as possible coupled into the device. Because the electrical response of the diode is quite slow, the stream of short pulses at 40 MHz essentially appear as continuous-wave light on the diode. Even when the pulses are not overlapping, the average power produces an offset in the voltage signal measured across the diode. However, the ultrafast dynamics are present for the short window where the pump and probe pulses overlap as shown in Figure 4.1.

This simple experiment served as an initial test of the experimental system. Although we cannot observe structure on a time scale less than 500 fs, a longer time constant is easily observed. From Figure 4.1, the exponential decay on the trace is on the order of 1 ps. This compares favorably with the results presented on previous devices similar to the one considered here [59]. As an initial test of the
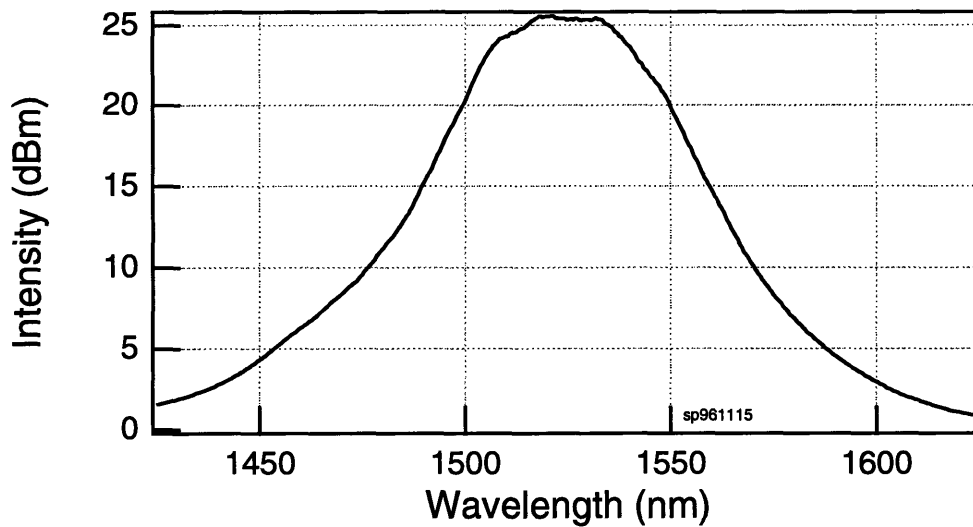
Figure 4.2   The spectrum of the MQW optical amplifier used in the pump-probe experiments in this chapter. The diode was biased at 30 mA and measured with an optical spectrum analyzer.

fiber laser as a source and of the techniques used to initially align the experiment, the voltage-bias data is a positive result.

4.2   Multiple Quantum Well GRIN-SCH Structures

In these experiments, we consider a typical MQW diode laser AR coated on both sides to produce an optical amplifier. The device is a InGaAsP/InP structure with three MQWs in a GRIN-SCH structure. For the particular device #1226C-4, which is 860 μm long, the photoluminescence was at 1.54 μm. On the chip several different waveguides are patterned, but only two are connected to a gold wire and pad for current injection. When the facets are in good condition, over 100 mA of current can be injected into the device without lasing. Although we inspect the facets each time the device is mounted, the facet quality is also tested by operating the device at a reasonably high current (100-150 mA). If the device begins to lase, which is easily visible on an optical spectrum analyzer, facet degradation is likely. On the device we studied, unfortunately, the facet of one of the waveguides was damaged, and a Fabry-Perot pattern was noted in the spectrum of the fiber laser after passing through it. Fortunately the facets on the remaining guide were in good condition, and the spectrum of the diode used in the following experiments is shown in Figure 4.2 for 30 mA of injected current. The center of the spectrum is at approximately 1525 nm, which gives a good estimate of the center of the gain peak.

For pump-probe measurements to yield useful results, it is essential that they be performed in a small signal regime. Additional nonlinearities created at high pump or probe powers could easily obscure the dynamics of the device. Although the average power used in pump-probe experiments is
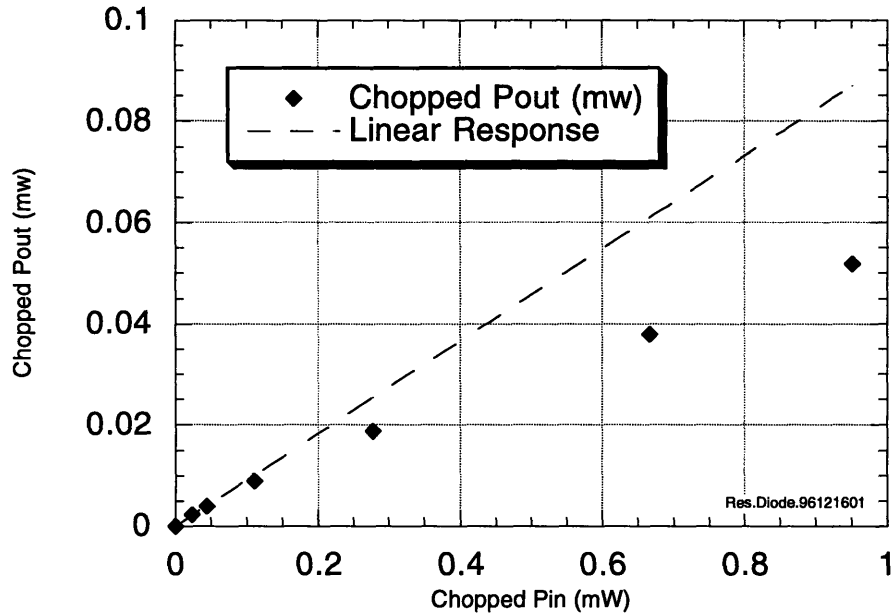
Figure 4.3   The chopped output power versus chopped input power for the diode used in the pump-
probe experiments in this chapter biased at 30 mA. The linear response is extrapolated from
the first three points.

often quite low, the peak power for the very short pulses can be quite high. When used in communica-
tions systems, the pulses are typically much longer, but the average power may be higher. For these
experiments we seek both an understanding of the physics of the semiconductor optical amplifiers and
a model for the ultrafast nonlinear optical characteristics that can be used in designing ultrafast optical
communication systems. Therefore to extrapolate the results obtained from pump-probe measure-
ments it is essential to be operating in a linear regime.

To test the linearity of the gain, we operated the optical amplifier at 30 mA and measured input
power before coupling into the device and output power after the beam passed through the device. A
fixed coupling loss was assumed, and since we were only seeking to test the linearity of the device it
was not necessary to measure the coupling loss. We operated the fiber laser modelocked with com-
pression and spectral filtering to fully simulate the experimental conditions. Only the pump beam was
measured, but since gain saturation effects are dependent on average power, the response for a single
beam is sufficient. The beam was chopped mechanically to differentiate the fiber laser signal from the
ASE produced by the diode. However, chopping also halves the power measured on the detector, so
for continuous-wave light both axes would be double. Figure 4.3 shows the measured response.

To insure zero input power corresponded to zero output power, a line without an offset was fit through
the first three points of the response, assuming that they were sufficiently small to maintain linearity in

the device. The divergence of the output from a linear response at higher input powers the becomes easily visible.

The measurement also provides the operating powers for the experimental system. From the input power measurement, approximately 2 mW (twice the measured value because of chopping) is the total power available for all the measurements presented here. However, it should be noted that the probe, reference, and pump must all be generated from the 2 mW. We measured the 2 mW immediately before coupling into the device, giving an indication of the losses present in the experimental system. Initially the fiber laser produces 40 mW, which reduces to approximately 10-12 mW after compression, and then 3-4 mW after spectral filtering. Additional losses from mirrors in the experimental system bring the total down to 2 mW before the device. This indicates that many aspects of the experimental system could be improved in terms of losses. However, from the graph it is also clear that most of the power is unnecessary because only one-tenth of the total power is needed to remain in the linear regime.

Figure 4.3 also indicates the type of output powers that must be detected. In the linear regime, an output signal less than 10 µW is reasonable, and this signal would include both pump and probe. 10 µW of signal average power corresponds to 250 fJ pulse energies for 100 fs pulses in the diode. Previously the short pulse saturation energy for similar MQW diode lasers with 150 fs pulses was measured to be 200 fJ [60, 61]. Assuming that the probe is just one tenth of the pump, the probe is on the order of 1 µW. Additionally, recall the reference and probe will be coupled into a fiber for final detection, so assuming that only 40% will be coupled, which is reasonable considering that the spatial mode after leaving the diode may not be ideal, 400 nW remains. On a typical detector this produces a signal on the order of 400 nA, so the signal levels are quite small.

As an aside, we note that this measurement demonstrates that it may not be absolutely necessary to maintain the pump significantly stronger than the probe. So long as the amplifier remains in the linear regime with the sum of the two signals, then the probe may be stronger than the pump and we could attain valid results. This can be quite useful because the measured signal may be increased substantially without altering the experimental results. In this experiment operating with a stronger probe would improve the signal-to-noise ratio, so it may be worth considering such an option when signal levels are low.

4.3   Transmission and Phase Measurements

The experiment was performed on the right side of diode #1226C-4 because the facets of the left side had been damaged. Before coupling into the diode, the polarization of pump and probe beams were measured by translating the input lens to direct the beams over the top of the diode. This would allow a measure of the polarization of the beams after passing through the short length of fiber and the

coupling optics. The various polarization combinations were noted, and the rejected ratios were also noted. Using a broadband polarizing beam splitting cube, we measured TE rejection on the order of 30:1, while TM rejection was on the order of 70:1 in both cases. The reasonable rejection ratios indicate that polarization is not rotated significantly in passing through the coupling fiber.

The linear response of the pump-probe traces was tested. Initially the total chopped output power after the diode was measured to be under 10 μW, as previously estimated from the linear response of the diode. We checked the linearity of the measured response in pump power by decreasing the pump by half while maintaining probe and reference power. Both transmission and phase magnitudes decreased by half, indicating the linear regime. To increase the measured signal, we made the probe larger than the pump, while keeping the total chopped power under 9 μW after the diode. The linearity was rechecked and the linearity remained, and the transmission changes were on the order of 5%.

The pump-probe delay was measured by taking an autocorrelation of both pump and probe pulses in the autocorrelator simultaneously. Since the Klinger mechanical stepper stage provides repeatable 6.7 fs steps, reasonable accuracy is possible. We placed a mirror just before the optics for coupling into the diode to direct the collinear pump and probe pulse stream into the autocorrelator. We measured the time interval between the pump and probe pulses by taking an autocorrelation. This interval could then be eliminated in known increments using steps of the Klinger stage. We overlapped the two pulses by changing the pump-probe delay to obtain the shortest autocorrelation of the sum of the two as measured by the FWHM. The measurement was done at the ideal polarization for the SHG crystal as oriented, which did not correspond to a pure polarization state incident upon the diode, but a mix of TE and TM polarizations. However, both pump and probe were at the same polarization. We estimate the error in this measurement to be on the order of 25 fs, or four steps of the Klinger stage.

In the measurements the HAM radio was used in FM demodulation for phase measurements and a Hewlett Packard spectrum analyzer was used in AM demodulation for transmission measurements. A BNC splitter was used to split the electrical signal from the tuned detector to both the radio and the spectrum analyzer. One lock-in amplifier detected each signal, and the output was acquired in LabView. We calibrated the phase measurement by modulating the mirror mounted on the PZT actuator with an amplitude which produced a known phase change. To preserve the calibration, no further adjustments were made on the gain, filtering, or center frequency of the radio receiver and spectrum analyzer.

Previously we had determined the approximate currents for gain, transparency, and absorption as 30 mA, 13 mA, and 3 mA. Data was collected for all four polarization combinations at each current setting. In switching between polarizations and currents we made as few changes as possible. In each case a pump polarization was set. Then reference and probe were changed through both polarizations by adjustment of only zero-order half-wave plates. We adjusted the polarization of the reference for

maximum beat signal in each case. We also adjusted the probe-reference delay each time for maximum beat signal. As the current was varied, the reference delay shifted because the index of the diode changes slightly with current injection. Figures 4.4-4.9 show the transmission and index data taken for all the various current and polarization combinations.

Curve fits to the data are shown in the same figures overlaying the data. The scheme used for fitting the data uses a recursive routine which includes a derivative of the phase for each transmission trace and a derivative of the amplitude for each phase trace to account for the spectral artifacts. Additionally, the slow and fast components were included to account for carrier heating, a delay in heating, and spectral hole burning. For the data presented here, 750 fs and 200 fs time constants produced the best fits across all the data. We inspected the amplitude of the various fitting components, but they did not appear to follow expected trends. For instance, at transparency the spectral hole burning contribution should be zero, but in some cases it was actually larger than its contribution in either absorption or gain. We believe that in some cases because the zero-delay-point is not well known the spectral hole burning contribution may mask the spectral artifact and vice-versa. Therefore lack of information about the zero-delay point prevents us from drawing quantitative conclusions about the contributions of the various components in this model. For this reason further fitting results will be discussed in the next section.

Qualitatively it is most reasonable to compare the data presented here with similar data obtained at the same wavelength with a heterodyne detection system creating similar percentage transmission changes. Previously, authors have noted that changes in incident power can affect the qualitative response of the device substantially [2]. G. Lenz obtained both transmission and phase data on strained-layer MQW devices, using a heterodyne technique and the F-Center laser for transmission changes on the order of 10% [4, 62]. A comparison between his results and these results show many similarities even though the devices he studied were considerably different. Although the signal-to-noise ratio is significantly better in the data presented here, both sets are qualitatively similar. In the gain regime for the phase change, the TM-TM case presented here demonstrates a negative-going change before becoming positive and decaying to a positive step change from stimulated transitions. In Lenz's data, the TM-TE case in gain shows the same feature. The transmission changes Lenz presented for the gain regime are quite similar to those we presented.

In our transparency data, the TE-TE case is particularly intriguing because of the significant influence of the spectral artifact. A similar structure was observed by Lenz in his transparency data. However, the structure he observed was significantly less sharp than it is in this data. In a later section we will discuss the possibility for fitting such a feature in more detail. The phase response Lenz obtained at transparency is qualitatively similar to those we show here. In the transparency data we note, as Hultgren did [2], the inconsistency between transparency points defined in terms of phase and transmission. In especially the TM-TM case, the transmission curve is clearly at transparency, while the phase curve is in absorption.
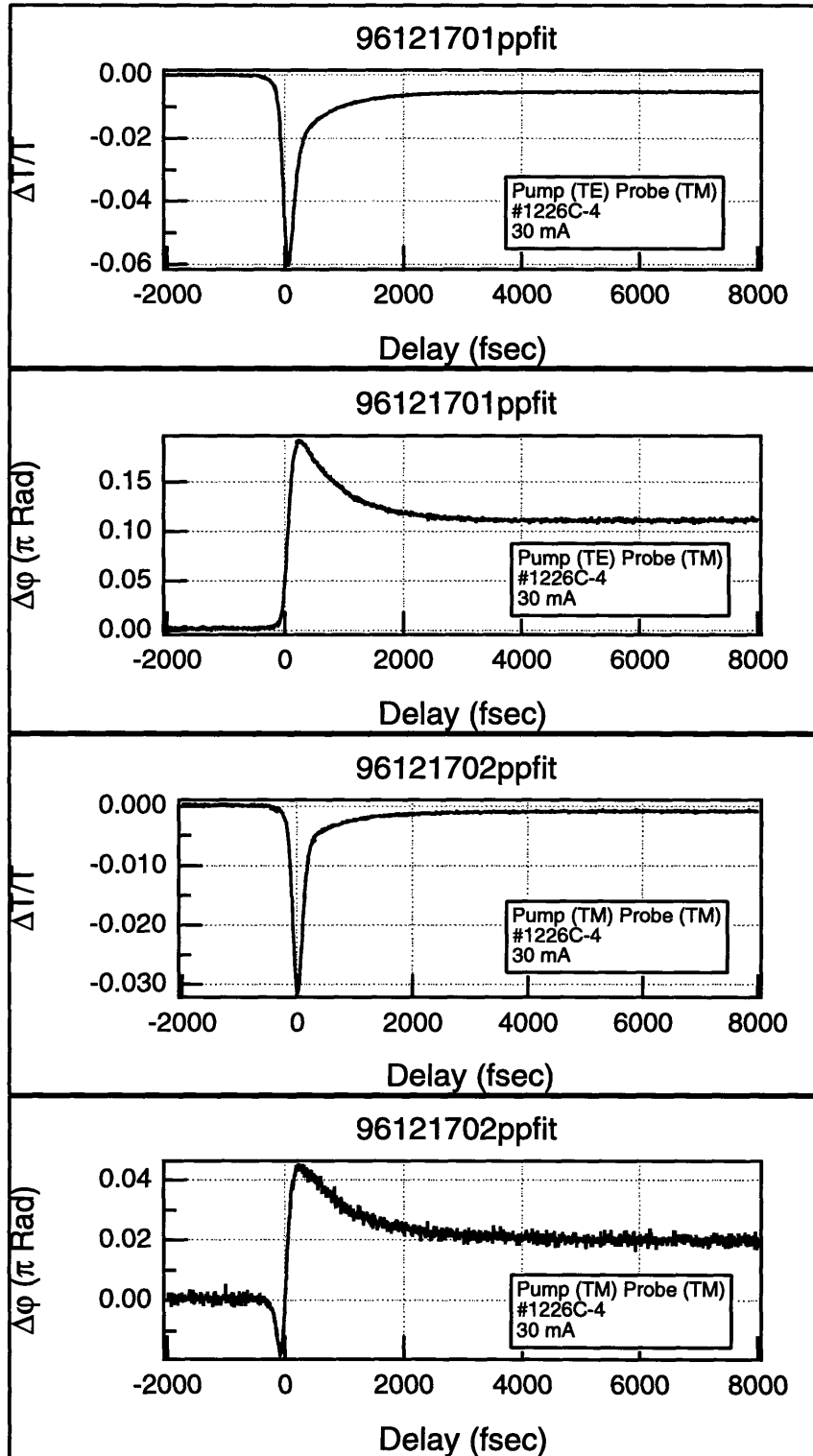
Figure 4.4   Transmission and phase measurements shown in pairs taken simultaneously in the gain regime with 30 mA injected. The pump and probe polarizations are indicated in the plots.
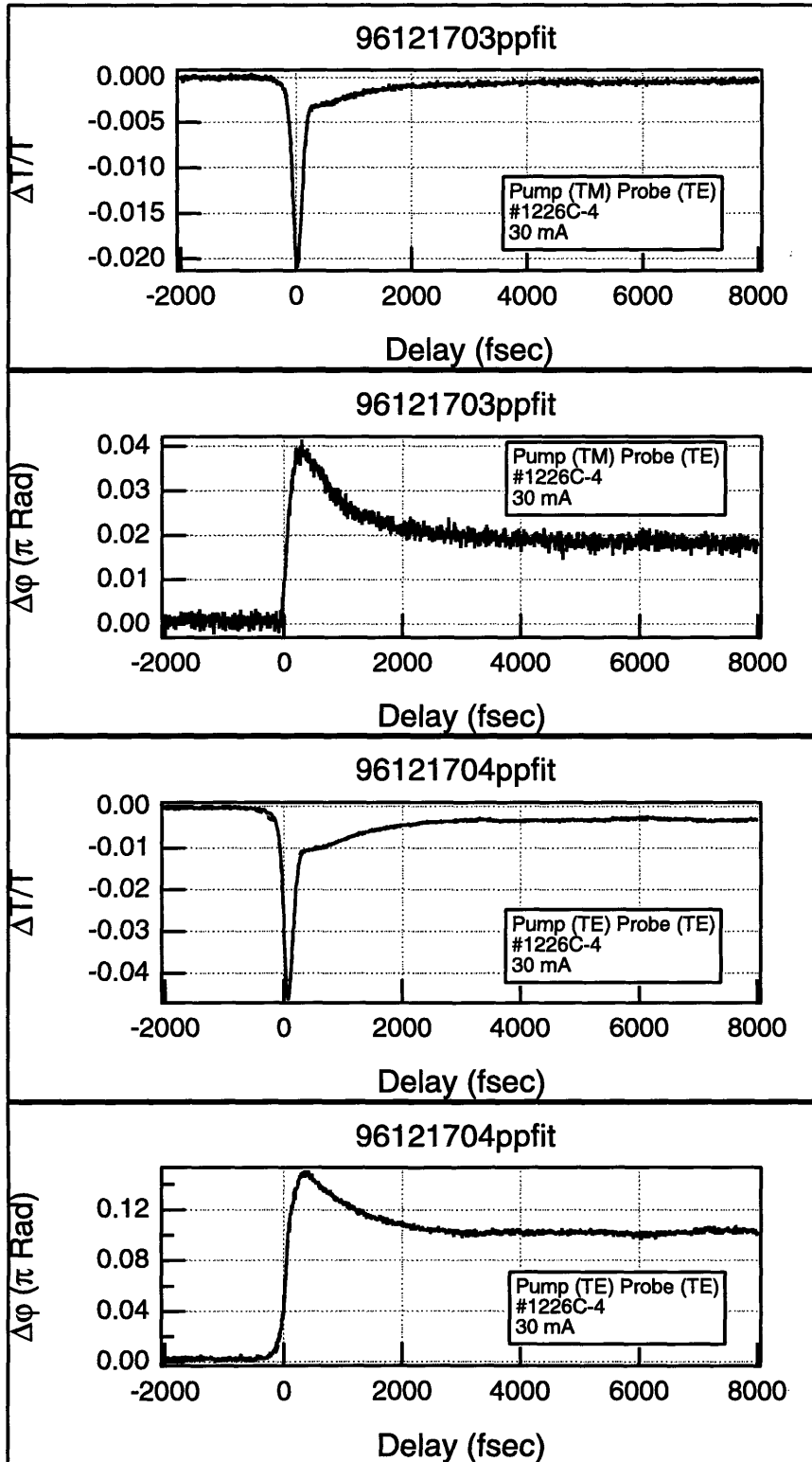
Figure 4.5   Transmission and phase measurements shown in pairs taken simultaneously in the gain regime with 30 mA injected. The pump and probe polarizations are indicated in the plots.
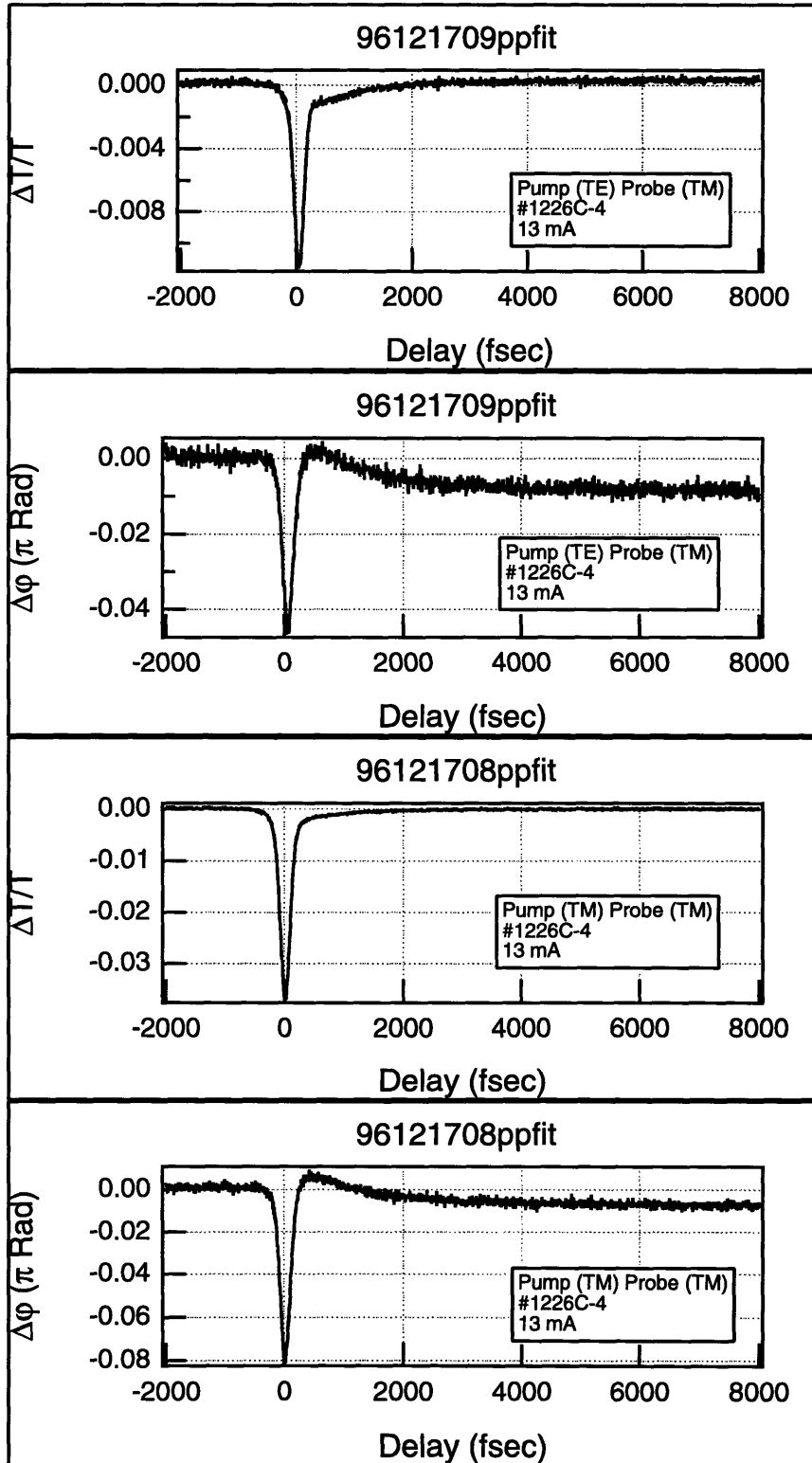
Figure 4.6   Transmission and phase measurements shown in pairs taken simultaneously in the transparency regime with 13 mA injected. The pump and probe polarizations are indicated in the plots.
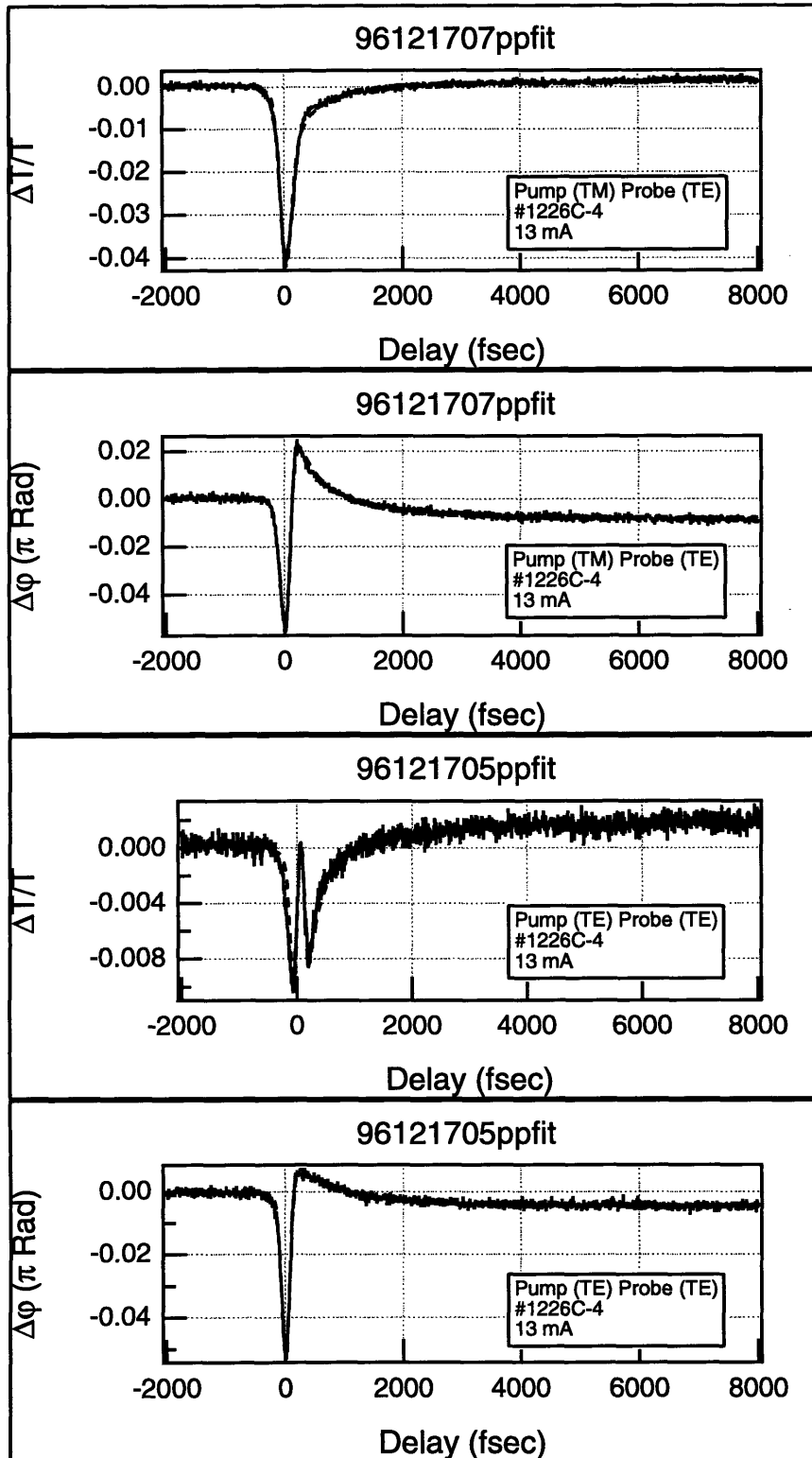
Figure 4.7   Transmission and phase measurements shown in pairs taken simultaneously in the transparency regime with 13 mA injected. The pump and probe polarizations are indicated in the plots.

Figure 4.8   Transmission and phase measurements shown in pairs taken simultaneously in the absorption regime with 3 mA injected. The pump and probe polarizations are indicated in the plots.
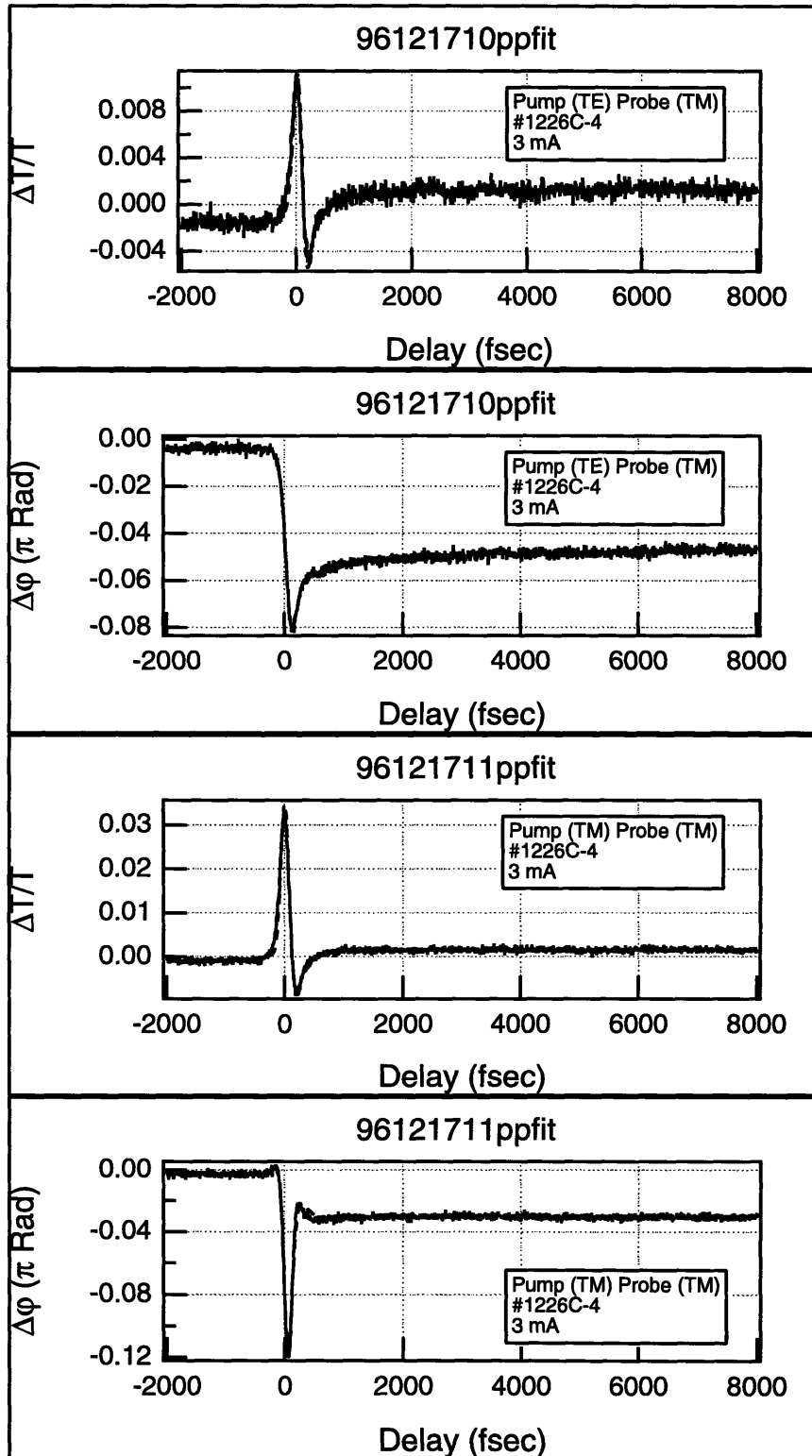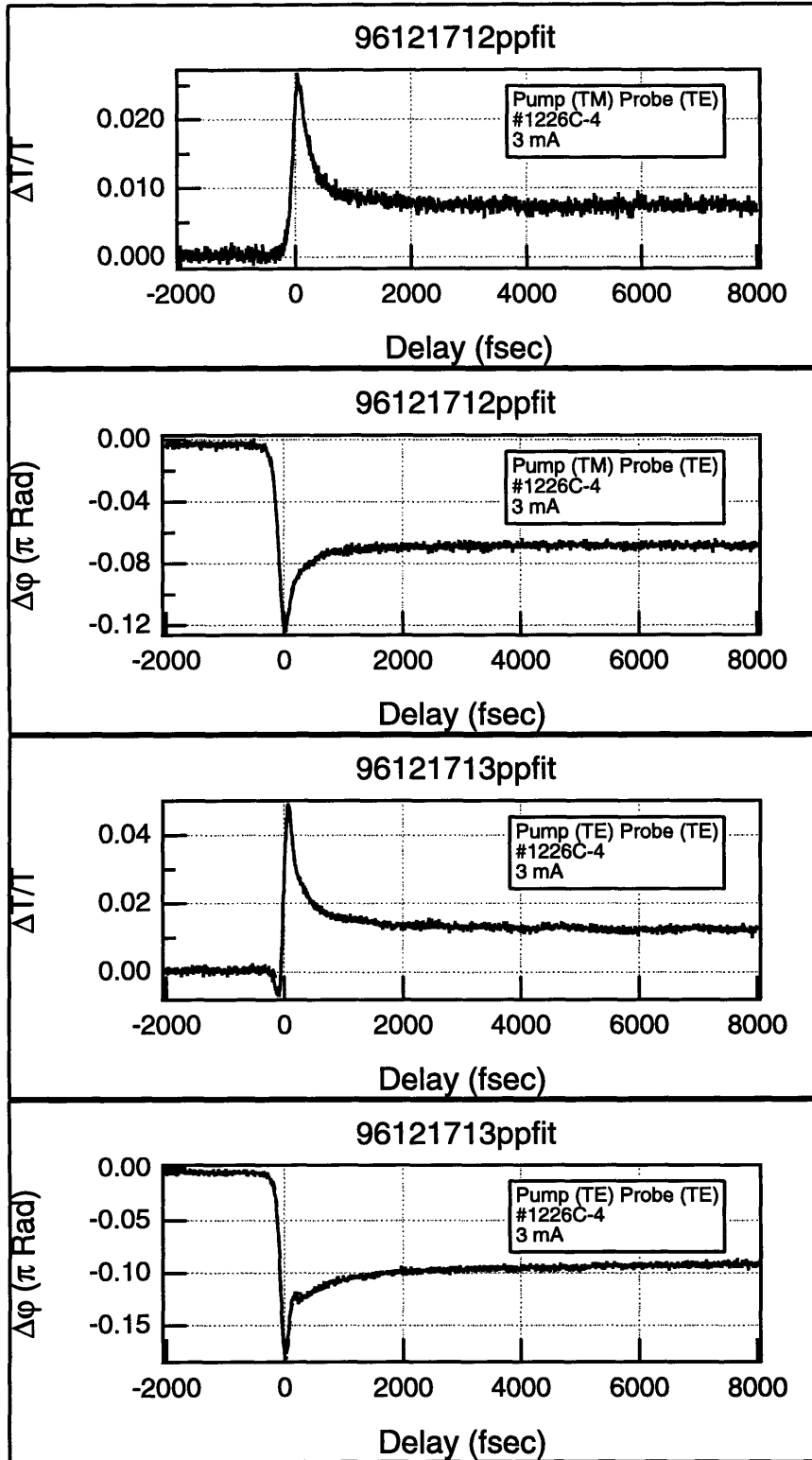
Figure 4.9   Transmission and phase measurements shown in pairs taken simultaneously in the absorption regime with 3 mA injected. The pump and probe polarizations are indicated in the plots.

In absorption Lenz's transmission results were similar for all polarization cases. In our results the TM-TE and TE-TE transmission responses are different from Lenz's because the sign of the carrier heating term is different. This may be due to the difference in device structure, but it is unclear. Our phase data in all but the TM-TM case has a very different signature from Lenz's data. Again the sign of the carrier heating component is different in our data than in Lenz's.

Although G. Lenz's data was obtained for a very different device structure, it is perhaps the most complete set of data available for comparison to the data presented here. We note several differences between the two data sets, but qualitatively the two are quite similar. From a cursory inspection, the data we obtained appears quite comparable to previous data in terms of general trends. However, the much better performance of the fiber laser and the detection system is evident in the comparison of the two data sets. Here we measure much smaller changes, with a better signal-to-noise ratio, revealing more features in the data. Transmission and phase results by other authors in similar InGaAsP laser diodes [3] as well as AlGaAs laser diodes [2, 63, 64] are qualitatively similar.

4.4   The Spectral Artifact

Because of the lack of a good measure of zero-delay, the initial fitting routine which used two time constants plus an artifact, produced difficult to interpret results. Therefore we simplified the model to a single time constant. For this simplified model, only the spectral artifact and TPA occur near zero-delay, so they are less likely to affect one another significantly. Based on the theory of the spectral artifact, we expect the contribution of the spectral artifact to scale with the slope of the gain [35]. The gain slope should become steadily steeper as the diode is operated further into the absorption regime. In the last section we used one long and one short time constant along with the spectral artifact, and we found that the short and long time constant combined to form a derivative-like structure which could sometimes mask the spectral artifact when the time shift was varied. Because of this, the influence of the spectral artifact could not be quantified. By only allowing a single long time constant, the spectral artifact fits all of the derivative structure in the data. Although a fit with an artifact term and a long time constant does not provide an excellent fit of all the data, it is reasonable.

To fit for the dependence of the spectral artifact, we chose the TE-TE data, which appeared to have the largest derivative component and would not exhibit pulse broadening by pulse walk-off [65]. We modified the recursive data fitting routine to first perform a two-time constant and spectral artifact fit of both phase and amplitude data. Since this result matches the data quite closely, we used these fits to calculate the artifact terms. Then both data sets were fit with a single long time constant and the calculated derivative. The data overlaid with fits for the three TE-TE cases are shown in Figures 4.10 and 4.11.
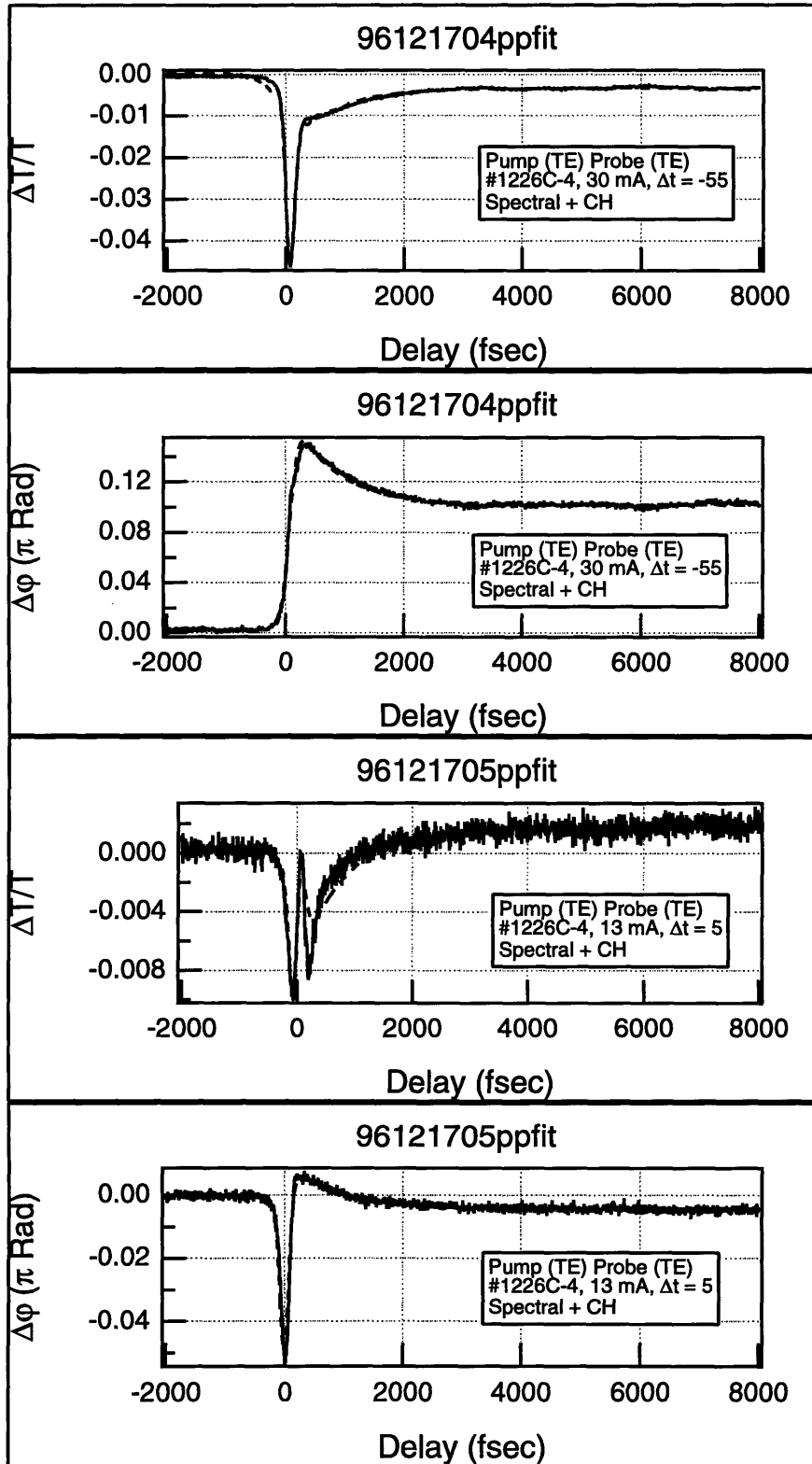
Figure 4.10 Transmission and phase data with pump and probe TE polarized and diode in gain and transparency with fits overlaid. Fits performed with spectral artifact and only a single long time constant.
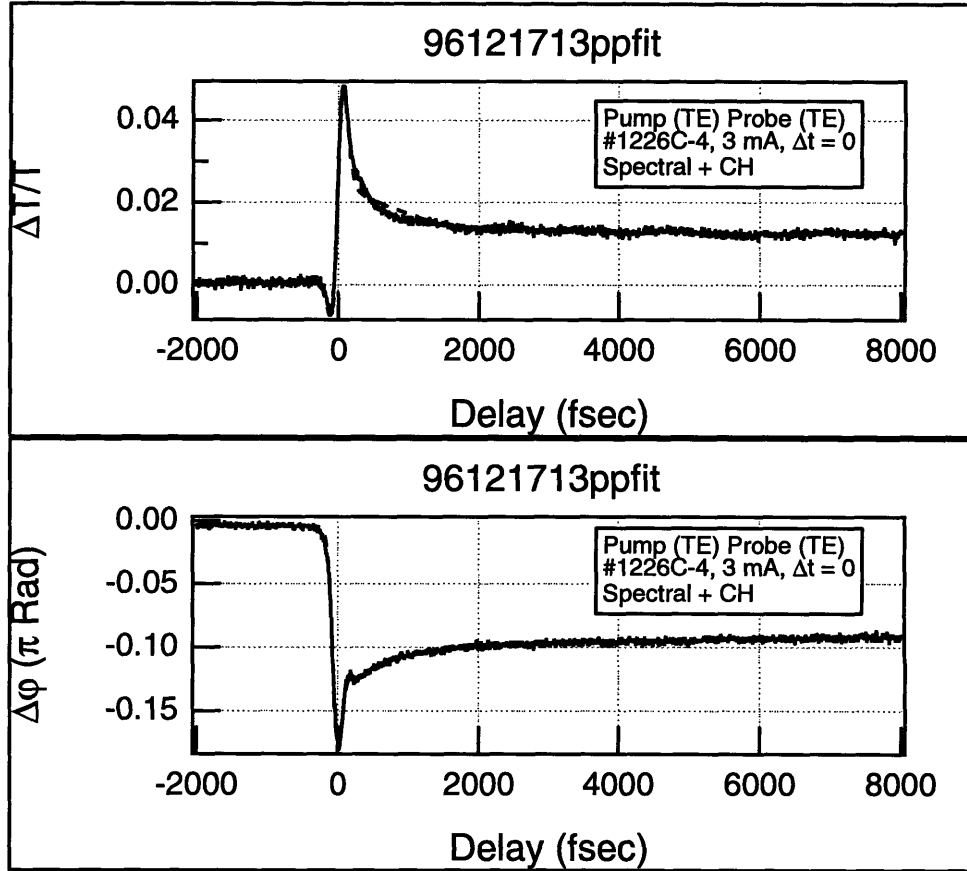
Figure 4.11 Transmission and phase data with pump and probe TE polarized and diode in absorption with fits overlaid. Fits performed with spectral artifact and only a single long time constant.

For the phase plots, the fits are quite good in all cases, but the fits for the transmission data are lacking across the data set. In transmission it appears clear that at least one additional component is needed for a good fit. We attempted fits with a pure delayed carrier heating model without spectral hole burning, where a short time constant was used in addition to the long time constant, but it was given the opposite sign of the carrier heating component. Although the fits were closer to the data, this model also did not succeed in completely fitting the data. In both cases, it appears that part of the problem is that we allow a time shift in all the fits. The value of the time shift was determined by min-imizing a sum of normalized error on both fits. Although we always obtained a time shift producing a minimum error, it varied between the various fitting procedures, which indicates that the fitted time shift is indeed artificial. Additional data on the exact position of zero time delay would allow much more consistent fitting of the data.

Even with the many fitting problems mentioned above, we noted a trend in the magnitude of the spectral artifact. We plotted the fast components of the simple fit using a single time constant and the spectral artifact term in Figure 4.12. At this time it is unclear how best to scale the spectral artifact term. In the fitting routine, the spectral artifact is calculated from the fit to phase data, which varies in

96121704ppcomp

ΔT/T

0.04
0.02
0.00
-0.02
-0.04
-0.06
-0.08

-1000   0   1000   2000   3000   4000

Pump (TE) Probe (TE)
#1226C-4, 30 mA, Δt = -55
Spectral + CH

Delay (fsec)

96121705ppcomp

ΔT/T

0.006
0.004
0.002
0.000
-0.002
-0.004
-0.006

-1000   0   1000   2000   3000   4000

Pump (TE) Probe (TE)
#1226C-4, 13 mA, Δt = 5
Spectral + CH

Delay (fsec)

96121713ppcomp

ΔT/T

0.02
0.01
0.00
-0.01
-0.02

-1000   0   1000   2000   3000   4000

Pump (TE) Probe (TE)
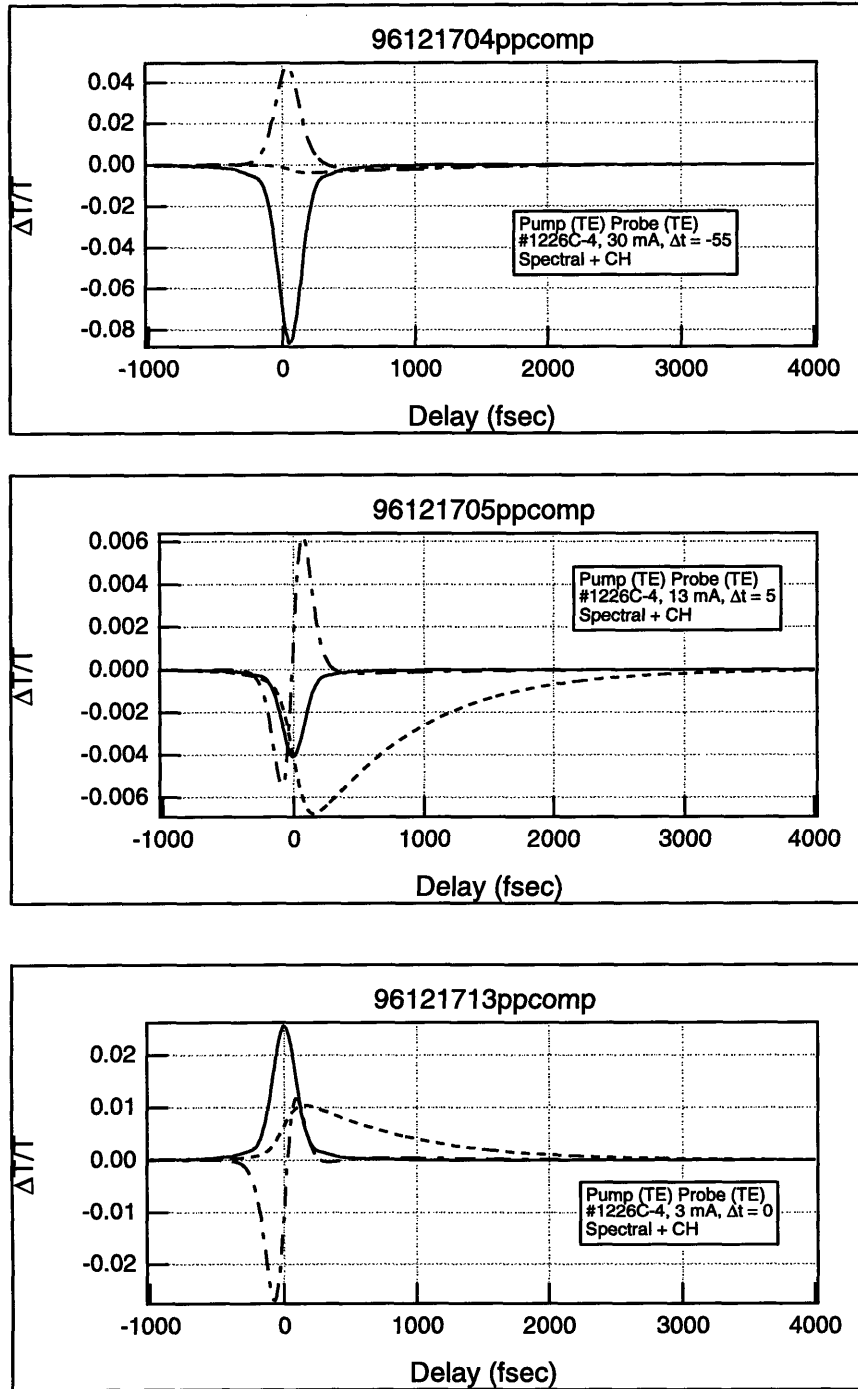#1226C-4, 3 mA, Δt = 0
Spectral + CH

Delay (fsec)

Figure 4.12   The TPA (solid line), spectral artifact (dash-dot line), and carrier heating (dashed line) components of the transmission fits from Figures 4.10 and 4.11. The importance of the spectral artifact appears to increase moving from gain (30 mA) to absorption (3 mA).

magnitude considerably for the various regimes. To eliminate this artificial variation its peak magnitude was normalized to one before fitting for the coefficient. However, this still does not produce coefficients that are properly scaled with respect to the other terms in the fit.

Inspection of the fast component data is somewhat promising. Relative to other components the spectral artifact is certainly smallest in the gain regime, where it is dwarfed by the delta function component. At transparency the spectral artifact becomes quite large and may even be relatively larger than it is in the absorption regime. However for these fits the most extreme data were selected, so this may be an unusual result at transparency. In this particular case it appears that the fitting algorithm artificially increased the spectral component to produce a better fit. If the appropriate additional term had been added to the fit and the zero-delay point was known, then the spectral artifact term may not be as large at transparency. If this is the case, then the contribution of the spectral component does exhibit the proper trend of increasing from gain into absorption.

We attempted several methods to quantify the change in the artifact contribution by following the analytical result by Mørk and Mecozzi [37] where they suggest that the magnitude of the spectral artifact relative to other direct contributions to the response should scale linearly with the slope of the gain curve. This cannot be done easily from the coefficients of the fit, so the resulting components shown in Figure 4.12 were used. The maximum value of the spectral artifact was divided by the maximum of the sum of all components except the spectral artifact. This did appear to produce coefficients which represented the trends visible in the component fits. The normalized spectral artifact contributions for the various regimes were 5.30E-1, 8.05E-1, and 6.75E-1 which correspond to gain, transparency, and absorption. Although the trend is not absolutely increasing, the extreme nature of the transparency data may be sufficient to explain the discrepancy.

4.5   Analysis Conclusions

Although we do not have a complete understanding of the data, we have been able to make several important advances. The implementation of simultaneous measurement of transmission and phase has been very successful and allows analysis that has not previously been possible. Because of these simultaneous measurements, we can curve-fit the spectral artifact for the first time experimentally. Although a number of theory papers have been written on the spectral artifact, no author has shown clear experimental results indicating its influence. Only through simultaneous measurement of both phase and transmission can derivatives between the two traces be calculated appropriately, so we have an excellent opportunity to provide such analysis.

The use of the fiber laser and the design of a new detection system has revealed a number of new features in the transmission and phase response. With a much more stable source and significantly better detection system, we have been able to guarantee that all measurements have been performed in the linear regime of the devices. From the results shown here, even operating above a 10% transmission change can produce some gain saturation. Considering the amplitude fluctuations present in color center lasers, measurements such as these would not have been possible. At the same time, the results shown here compare favorably with results obtained by G. Lenz using a F-center laser system.

Analysis of the data has shown that the zero-delay point must be known for exact fitting of the data. As mentioned, although several different fitting models were used, each would produce a different time shift, indicating the uncertainty in the result. If the zero-delay point were fixed, then several fitting models could probably be ruled out to produce a physical explanation of the data. This determination of zero-delay for each trace may be possible experimentally, and considering these results we will pursue its implementation.

Here we have considered the extremes in possible fitting algorithms. A fit with a single time constant and the spectral artifact is clearly oversimplified because it neglects the delay in carrier heating and spectral hole burning, which are both predicted theoretically. On the other hand, a fit with a short and long time constant and the spectral artifact represents an overspecified model, where too many parameters have been attempted with insufficient data, so the results are inconclusive. Perhaps with a clear measurement of zero-delay, a physically sensible fit will become possible that is between the two extremes attempted here.

Even in the most extreme case of TE-TE data, the spectral artifact does exhibit some of the predicted trends. Again these are the first measurements where the spectral artifact can even be considered because both phase and transmission data are available which were obtained simultaneously. Even with both transmission and phase data present, the lack of an exact measure of zero-delay may prevent the complete analysis. Still, the trends are promising for exactly characterizing the spectral artifact and then eliminating it in the data analysis. As an alternative to such analytical elimination of the spectral artifact, we consider in the next chapter the experimental elimination of the spectral artifact.

CHAPTER 5: EXPERIMENTAL ELIMINATION OF SPECTRAL ARTIFACTS

In the last chapter we attempted to extract the magnitude of the spectral artifact from pump-probe data obtained using a heterodyne technique. Unfortunately we could not draw a clear conclusion, possibly because of lack of information about zero-delay. If we can obtain this experimentally, fitting analysis of the spectral artifact may be possible leading to an understanding other pump-probe components, such as spectral hole burning and a delay in carrier heating. However, because spectral hole burning and a delay in carrier heating may occur on the same time scale as the spectral artifact, even when the zero time delay is known we may not be able to fit the data any better than we can currently. For this reason it is important to consider experimental methods for eliminating the spectral artifact.

5.1   Measurement of the Gain Slope

Physically, the spectral artifact is the result of the slope on the gain curve. The gain spectrum of an optical amplifier, or virtually any semiconductor device, acts as a filter for the spectrum travelling through the device. If the device produces an instantaneous change in phase, the corresponding shift in frequency is filtered by the gain, producing an amplitude artifact. The size of this artifact will then be directly proportional to the slope of the gain, to lowest order. However, a filter is really just a linear element, so an additional filter could be added to cancel the effect of the gain filter. Experimentally it may be difficult to create such a filter, but such a simple idea could be a method for significantly reducing the effect of the artifact.

Initially it is useful to compare the full fiber laser spectrum to a calculated gain spectrum. Although we have only outlined how to calculate the gain curve in a very crude form, we have also shown that it can still provide a great deal of physical insight. Figure 5.1 shows a typical fiber laser
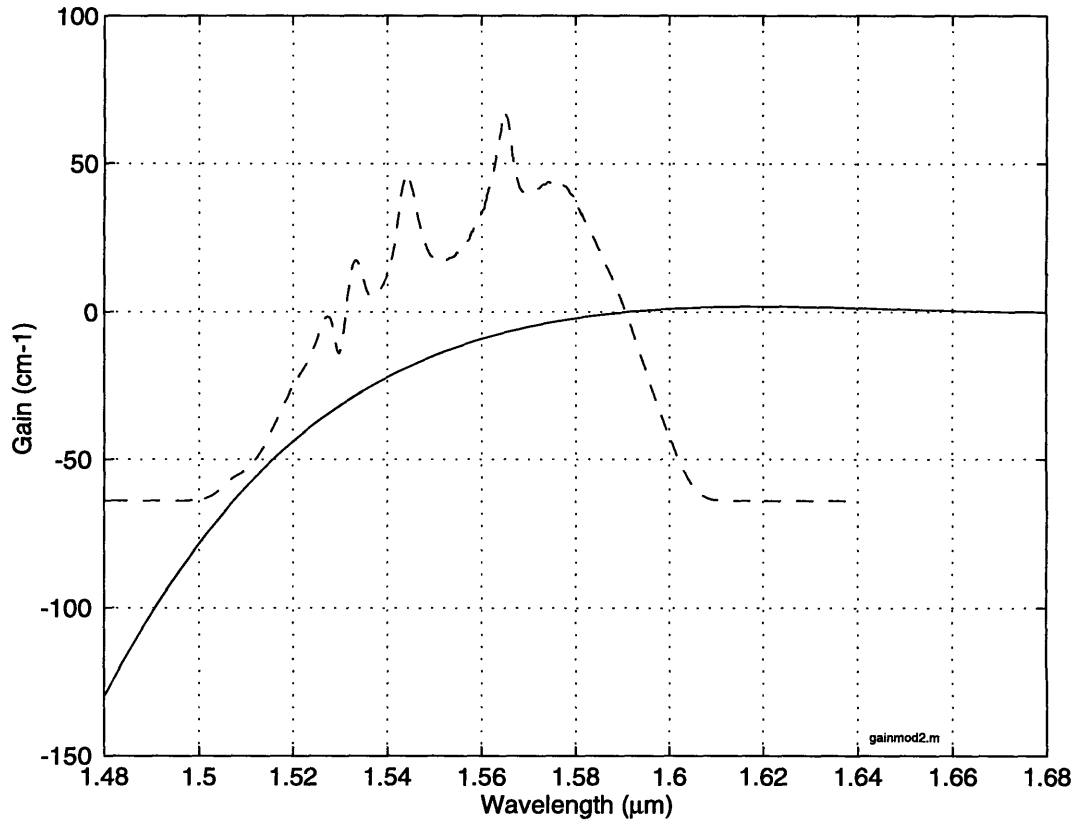
Figure 5.1   A measured modelocked fiber laser spectrum without spectral filtering superimposed on a gain
curve calculated versus wavelength using the constants defined in Chapter 2.

spectrum compared to a calculated gain spectrum using parameters similar to those in Chapter 2. To correspond to the measurement of the diode output spectrum in the last chapter, the gain peak should be centered at a shorter wavelength. However, the figure does illustrate the breadth of the full fiber laser spectrum. Considering that approximately one-third of the spectrum would be used in a pulse in the experiment after spectral filtering, the tuning range may be sufficient to go between diode regimes. The figure also shows that the gain slope may not be linear over the pulse spectrum, so filtering to eliminate the artifact might be quite complicated.

With at least a picture of the range of operating wavelengths and general shape of the gain curve, we need an experimental estimate of the real gain slope. One method to measure the gain slope is to consider the change on the spectrum of the pulses passing through the diode. We measured the change in spectrum of the pump beam coupled through the diode. After passing through the diode, we coupled the pump into the fiber used in the heterodyne detection, and a fiber-coupled optical spectrum analyzer measured the spectrum. For each current setting of the diode, we measured the spectrum of the pump beam passing through the diode and the amplified spontaneous emission (ASE) from the diode without the pump beam present. Since only the slope was needed, all measurements were made
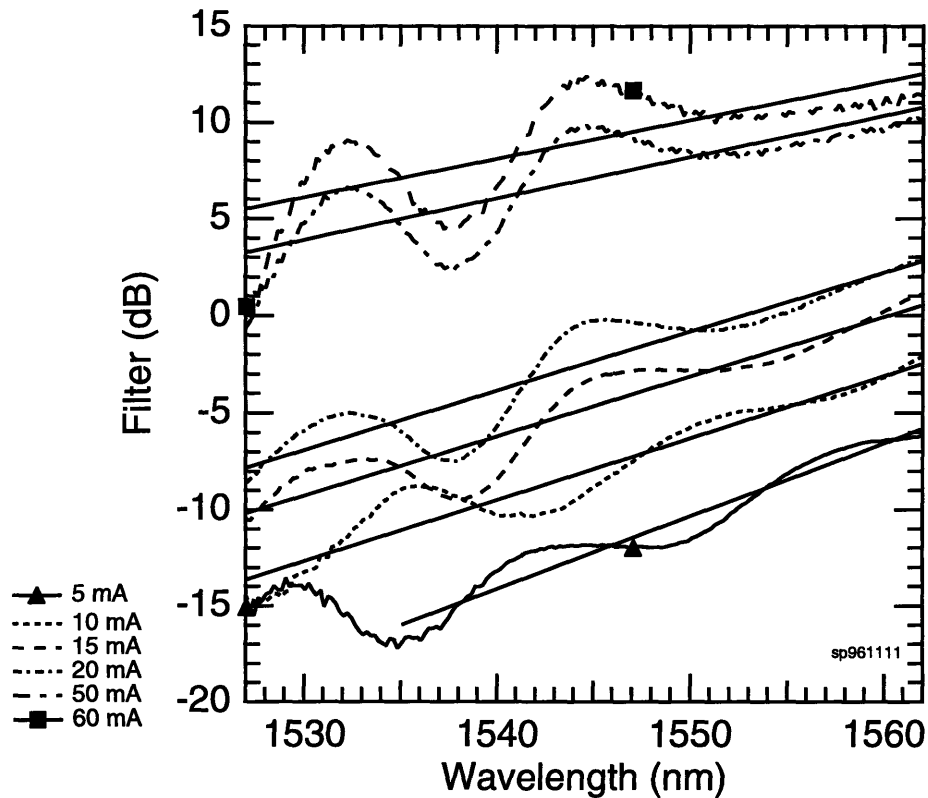
Figure 5.2   The filtering of the diode for several wavelengths and injection currents measured by comparing the modelocked fiber spectrum input and output from the diode while subtracting amplified spontaneous emission at each current. Linear curve fits superimposed on the data estimate the gain slope over the shown wavelength range. The ripples are due to Fabry-Perot effects.

on a logarithmic scale. To obtain a pump spectrum not affected by the diode, the lens used to couple into the diode was raised so that the pump beam went over the top of the diode, without passing through it. This allowed the pump beam to still pass through all the same coupling elements, but not pass through the diode itself. This spectrum was then used as the reference.

For each current setting, the spectrum of the ASE from the diode was subtracted from the spectrum measured with both the pump and ASE present. Then the result was divided by the pump input spectrum to obtain the filter function as shown in Figure 5.2. To estimate the slope, linear fits are shown in the figure over a small portion of the spectrum near the range where measurements would typically be taken. The slope behaves as expected, with a steeper slope at lower current. From transmission measurements, 15 mA was approximately where transparency occurred. The undulations in the curves are due to Fabry-Perot effects observed in the diode. This was later found to be due to front facet damage which was likely caused by atmospheric degradation. However, even with the Fabry-Perot effects, the linear fits provide an estimate of the gain slope.
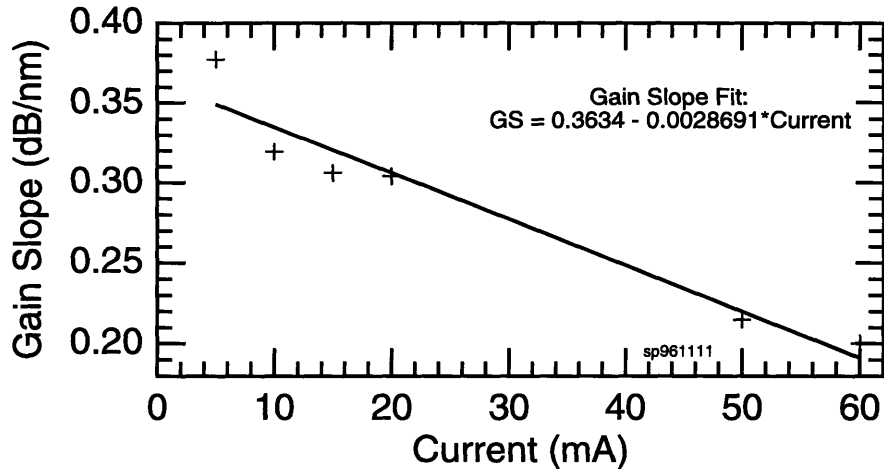
Figure 5.3   An estimate of the gain slope from linear curve fits to the experimentally determined filter function as a function of injection current. A linear curve fit is superimposed for estimating the slope at unmeasured injection currents.

Figure 5.3 shows the slope obtained from the linear fits at each current. Although not exactly accurate, a simple linear fit of the gain slopes is shown on the figure to provide an interpolated estimate of the gain slope at all currents. As a first estimate of the gain slope, the measurement is quite convincing. Although the accuracy of the values is somewhat questionable, especially considering the Fabry-Perot effects that were noted, the trend is appropriate. The diode used for all the transmission and phase measurements presented here was the second diode on this particular chip, which did not exhibit the Fabry-Perot effects discussed here.

5.2   Filtering to Eliminate Artifact

Since the gain will act as a linear filter, designing another filter to exactly compensate the gain slope would eliminate the spectral artifact. In selecting a filter we must consider the slope of the filter and the center of the filter. Ideally a single filter could be adjusted to compensate for all currents corresponding to each gain regime. One option is to consider an interference filter, similar to the one used in the spectral filter of the fiber laser pulses described in Chapter 3. Since the filter function varies slowly across the spectrum in a hyperbolic secant shape, the slope also varies considerably. By shifting the center wavelength, the slope can be set at a particular wavelength. For such a filter to work, the bandwidth and center wavelength must be picked to produce the desired response. We can model the filter and the type of gain slope that we expect using the data shown in the last section to estimate the gain slope, the derived gain function of Chapter 2, and specifications on 30 nm interference filters.

Interference filters can be designed with a variety of shaping functions, but the smoothest appears to be a double cavity filter, which produces the hyperbolic secant shape used in the spectral fil-
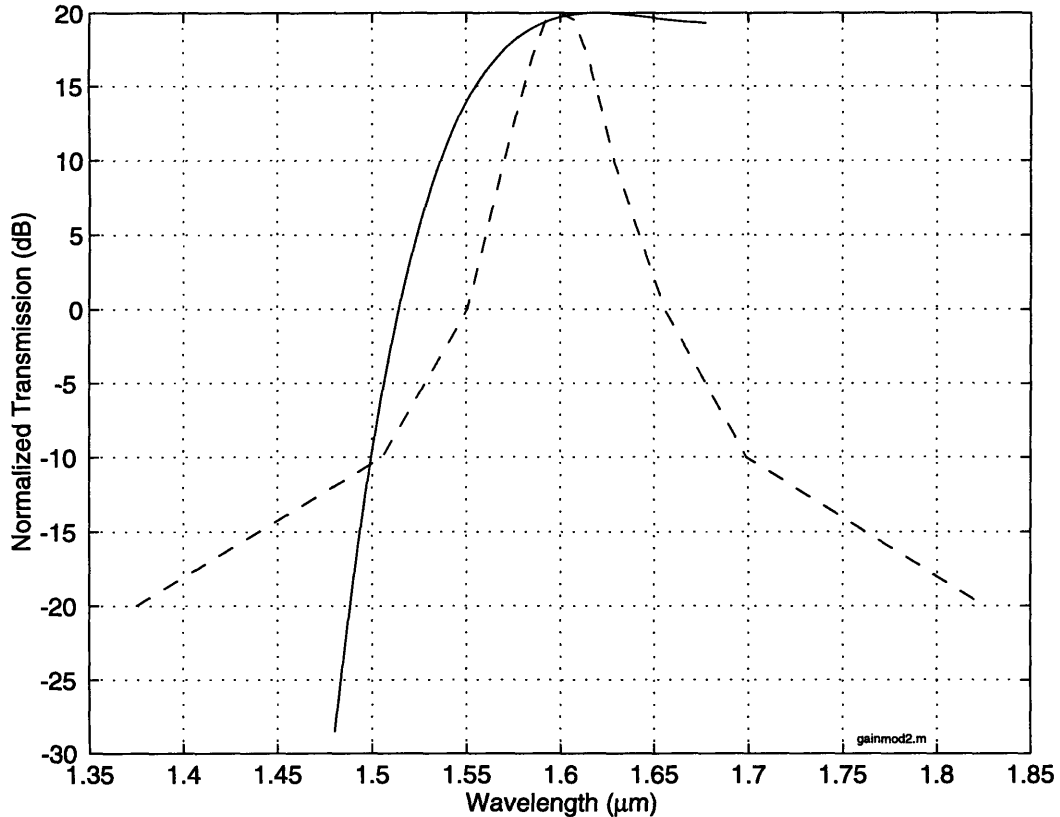
Figure 5.4   A gain slope calculated from the parameters of Chapter 2 and the spectral response of a 30
nm interference filter superimposed for comparison.

tering. The smoothness is important so that the derivatives will change gradually. Figure 5.4 shows a
double cavity 30 nm wide interference filter centered at 1.6 μm plotted on the same filtering scale as a
calculated gain curve using the theory and parameters from Chapter 2 with a transparency point around
1.6 μm. The plotted filter function was generated with only the few points which are specified by the
manufacturer, but in reality would be smooth throughout. Inspecting the plot shows that the slopes of
the two curves are at least similar, so it may be a suitable filter.

As a more quantitative analysis of the filter response, we calculated numerical derivatives of
both the theoretical gain curve and the filter function. Figure 5.5 displays the derivatives of the gain
and filter functions shown in Figure 5.4. Because only a few points are available in the filter function,
the large derivatives are not very smooth, but they still provide a range of the possible gain slopes. The
values shown on the figure may then be compared to the experimentally obtained results of Figure 5.3.
Experimentally the gain slope was measured between 0.2 - 0.4 dB/nm, and Figure 5.5 shows the filter
slope could compensate this range of gain slopes. So the interference filter appears to be a viable alter-
native. However, we note that to obtain the required slope the filter would be operated in the wings,
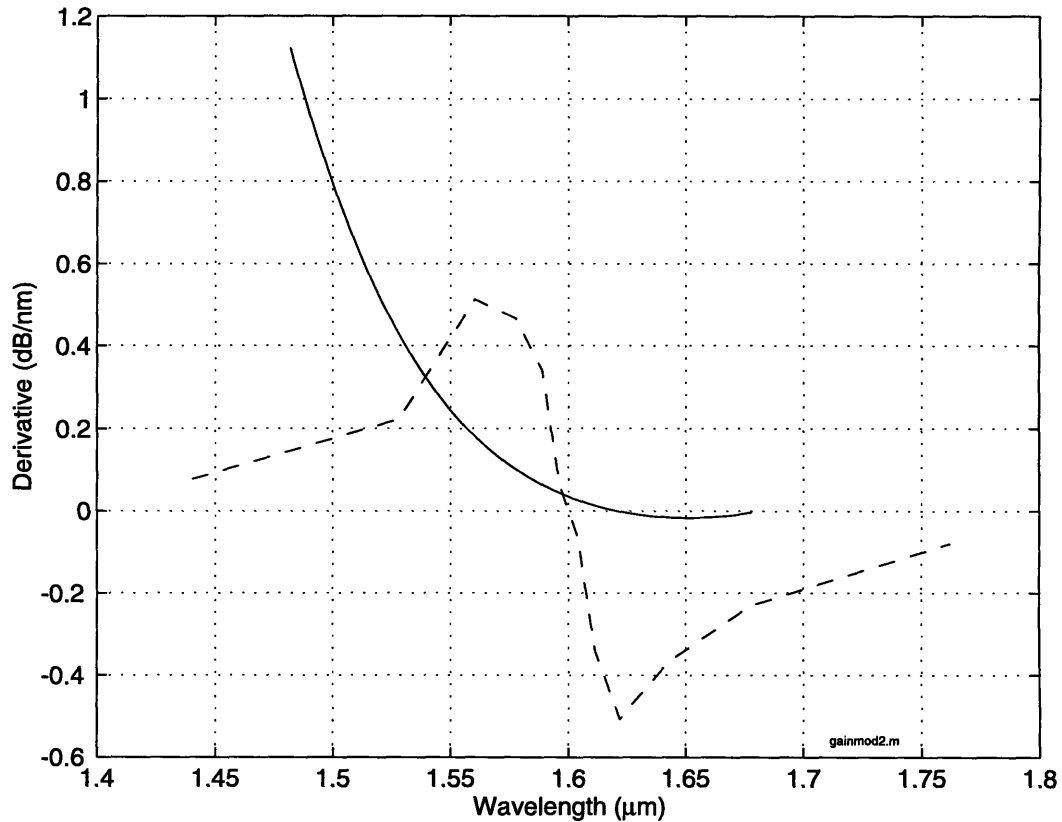
Figure 5.5   Numerical derivatives of the gain and spectral response of the 30 nm interference filter shown in Figure 5.4. Since only a few points were available for the interference filter, the derivative is unsmooth.

where the transmission is the lowest. Depending on the size of the signal and the noise floor of the detection system, this may or may not prove to be a feasible alternative in these measurements.

From this analysis an interference filter may be useful in experimentally eliminating the spectral artifact. By considering theoretical results of gain calculations compared to experimental measurements, we have concluded that an interference filter may compensate gain filtering, thereby eliminating the spectral artifact. However, the procedure may be impractical in an experimental setting because of the loss of the filter as it would have to be tuned for low transmission. However, the analysis here is by no means exhaustive. There are several other methods that may be used for filtering which could give completely arbitrary filter functions. For instance a liquid crystal modulator between a grating compressor could realize an arbitrary filter function. However, in such a system loss would remain an issue. Still other alternatives should be considered for eliminating the spectral artifact because it clearly affects pump-probe results quite significantly.

CHAPTER 6: CONCLUSIONS

Although this thesis has not experimentally resolved the issue of the importance of the spectral artifact in pump-probe measurements, it has overcome a number of the experimental obstacles to direct observation of the artifact. We have demonstrated that the stretched-pulse erbium-doped fiber laser is an excellent source for heterodyne pump-probe measurements near 1.5 μm. However, several advances could be made in the source. Several authors have reported stretched-pulse lasers with output powers near 100 mW by using longer lengths of erbium fiber and reverse pumping. For shorter pulses, the non-rejected APM output could be used directly for the experiment, assuming that compression losses could be reduced. Since wavelength tuning using spectral filters would reduce power levels considerably, the possibility of an erbium amplifier for the output of the fiber laser might make a fully tunable source possible. In all of these possible configurations some variant of the stretched-pulse fiber laser could be used, but new features would be accessible.

Although the development of simultaneous measurement of amplitude and phase is a simple modification, it is a significant step toward understanding the spectral artifact. Although the results here suggest that such synchronized data are still insufficient for resolving the artifact, it is a first step. Detecting the coherent beat frequency of the pump and probe would be one way to measure the zero time delay position quite accurately. This method would be quite accurate for co-polarized beams, but would be somewhat problematic for cross polarized measurements where the average zero-delay will occur at an unknown point in the diode. Although bias-monitoring typically requires high incident power, it would be the ideal method for determining zero-delay since it would pinpoint the delay within the diode for both cross and copolarized measurements. Adding a more accurate determination of zero-delay is the next step in resolving the spectral artifact.

Once the spectral artifact can be resolved through analysis, its dependence should be verified experimentally. The simple measurement of the gain slope presented here is a first step, but a more accurate method is desirable. One possible method would be to modulate the current injection to the

diode, pass a beam through it, reflect the beam off a grating to spatially separate the wavelengths, and then detect with a balanced difference detector. The balanced detector would detect the shift of the wavelength as a function of current injection. The current modulation frequency could be used to lockin-detect changes in the wavelength shift. Measurements at various bias currents would then provide a relative measurement of the gain curve. This measurement could then be calibrated to spectral measurements similar to those in Chapter 5 used to estimate the gain slope. Then using the results of analysis of a full data set, the dependence of the spectral artifact on injection current could be compared to an experimental prediction.

Finally, experimental elimination of the spectral artifact would be ideal. However, such a task appears quite difficult to perform given the width of the spectrum to be compensated and the range of gain slopes to be compensated. Still if such experimental compensation is possible, then a wide range of new measurements are possible and the true physical processes could be resolved. Certainly at that point short pulse experiments would become much more interesting, especially in a co-polarized case where polarization walk-off is not significant.

We have made significant progress in our understanding of the spectral artifact in this thesis, but a great deal of work remains. From the data we presented, a number of areas for improvement have been identified. Experimentally some of the issues are quite difficult, but others are relatively easy to implement. In the long term, understanding of the spectral artifact will be essential for discerning ultrafast processes on time scales below 500 femtoseconds.

REFERENCES

[1]   K. L. Hall. Femtosecond nonlinearities in InGaAsP diode lasers. MIT Doctoral Thesis. May 1993.

[2]   C. T. Hultgren. Femtosecond nonlinearities in AlGaAs diode laser amplifiers. MIT Doctoral Thesis. July 1994.

[3]   K. L. Hall, G. Lenz, A. M. Darwish, and E. P. Ippen. Subpicosecond gain and index nonlinearities in InGaAsP diode lasers. Optics Communications. vol. 111, pp. 589-612, 1994.

[4]   G. Lenz. Femtosecond sources at 1.5 microns and their application for time-resolved spectroscopic studies of semiconductor devices. MIT Doctoral Thesis. December 1995.

[5]   E. P. Ippen and C. V. Shank. Techniques for measurement. in Ultrashort Light Pulses, Picosecond Techniques and Applications. vol. 18, S. L. Shapiro, ed., pp. 83-122, Springer-Verlag, New York, 1977.

[6]   G. P. Agrawal. Population pulsations and nondegenerate four-wave mixing in semiconductor lasers and amplifiers. Journal of the Optical Society of America B. vol. 5, no. 1, pp. 147-158, 1988.

[7]   J. Zhou, N. Park, J. W. Dawson, K. J. Vahala, M. A. Newkirk, and B. I. Miller. Terahertz four-wave mixing spectroscopy for study of ultrafast dynamics in semiconductor optical amplifier. Applied Physics Letters. vol. 62, p. 2301, 1993.

[8]   N. W. Ashcroft and N. D. Mermin. Solid State Physics. Saunders College, Philadelphia, 1976.

[9]   C. Weisbuch and B. Vinter. Quantum Semiconductor Structures. Academic Press, Boston, 1991.

[10] H. C. Casey and M. B. Panish. Heterostructure Lasers, Part A: Fundamental Principles. Academic Press, New York, 1978.

[11] J. I. Pankove. Optical Processes in Semiconductors. Prentice-Hall, Englewood Cliffs, NJ, 1971.

[12] D. C. Hutchings, M. Sheik-Bahae, D. J. Hagen, E. W. Van Stryland. Kramers-Kronig relations in nonlinear optics. Optical Quantum Electronics. vol. 24, pp. 1-30, 1992.

[13] J. Manning, R. Olshansky, and C. B. Su. The carrier-induced index change in AlGaAs and 1.3 μm InGaAsP diode lasers. IEEE Journal of Quantum Electronics. vol. 19, no. 10, pp. 1525-1530, 1983.

[14] B. R. Bennett, R. A. Soref, and J. A. del Alamo. Carrier-induced change in refractive index of InP, GaAs, and InGaAsP. IEEE Journal of Quantum Electronics. vol. 26, no. 1, pp. 113-122, 1990.

[15] C. H. Henry, R. A. Logan, and K. A. Bertness. Spectral dependence of the change in refractive index due to carrier injection in GaAs lasers. Journal of Applied Physics. vol. 52, no. 7, pp. 4457-4461, 1981.

[16] H. Haug and S. W. Koch. Quantum Theory of the Optical and Electronic Properties of Semiconductors. 2nd Ed. pp. 44-47, World Scientific, New Jersey, 1993.

[17] G. Bastard. Wave mechanics applied to semiconductor heterostructures. Halsted Press, New York, 1988.

[18] K. Vahala, L. C. Chiu, S. Margalit, and A. Yariv. On the linewidth enhancement factor α in semiconductor injection lasers. Applied Physics Letters. vol. 42, no. 8, pp. 631-633, 1983.

[19] N. K. Dutta. Calculate absorption, emission and gain in $In_{0.72}Ga_{0.28}As_{0.6}P_{0.4}$. Journal of Applied Physics. vol. 51, no. 12, pp. 6095-6100, 1980.

[20] G. Eisenstein, R. S. Tucker, J. M. Wiesenfeld, P. B. Hansen, G. Raybon, B. C. Johnson, T. J. Bridges, F. G. Storz, and C. A. Burrus. Gain recovery time of traveling-wave semiconductor optical amplifiers. Applied Physics Letters. vol. 54, no. 5, pp. 454-456, 1989.

[21] P. Rees, H. D. Summers, and P. Blood. Gain-current calculations for bulk GaInP lasers including many body effects. Applied Physics Letters. vol. 59, no. 27, pp. 3521-3523, 1991.

[22] W. H. Knox, D. S. Chemla, G. Livescu, J. E. Cunningham, and J. E. Henry. Femtosecond carrier thermalization in dense Fermi seas. Physical Review Letters. vol. 61, no. 11, 1290, 1988.

[23] M. Sheik-Bahae and E. W. Van Stryland. Ultrafast nonlinearities in semiconductor laser amplifiers. Physical Review B. vol. 50, pp. 14171-14178, 1994.

[24] A. Grabmaier, M. Schofthaler, A. Hangleiter, C. Kazmierski, M. Blez, and A. Ougazzaden. Carrier transport limited bandwidth of 1.55 μm quantum-well lasers. Applied Physics Letters. vol. 62, no. 1, p. 10-13, 1993.

[25] R. Nagarajan, T. Fukishima, M. Ishikawa, J. E. Bowers, R. S. Geels, and L. A. Coldren. Transport limits in high-speed quantum-well lasers: Experiment and theory. IEEE Photonics Technology Letters. vol. 4, no. 2, pp. 121-123, 1992.

[26] N. Tessler and G. Eisenstein. Distributed nature of quantum-well lasers. Applied Physics Letters. vol. 62, no. 1, p. 10-13, 193.

[27] K. L. Hall, G. Lenz, E. P. Ippen, U. Koren, and G. Raybon. Carrier heating and spectral hole burning in strained-layer quantum-well laser amplifiers at 1.5 μm. Applied Physics Letters. vol. 61, no. 21, pp. 2512-2514, 1992.

[28] M. S. Stix, M. P. Kesler, and E. P. Ippen. Observations of subpicosecond dynamics in GaAlAs laser diodes. Applied Physics Letters. vol. 48, no. 25, pp. 1722-1724, 1986.

[29] M. P. Kesler and E. P. Ippen. Subpicosecond gain dynamics in GaAlAs laser diodes. Applied Physics Letters. vol. 51, no. 22, pp. 1765-1767, 1987.

[30] K. L. Hall, J. Mark, E. P. Ippen, and G. Eisenstein. Femtosecond gain dynamics in InGaAsP optical amplifiers. Applied Physics Letters. vol. 56, no. 18, pp. 1740-1742, 1990.

[31] C. S. Menoni, O. Buccafusca, M. C. Marconi, D. Patel, J. J. Rocca, G. Y. Robinson, and S. M. Goodnick. Effect of indirect G-L and G-X transfer on the carrier dynamics of InGaP/InAlP multiple quantum wells. Applied Physics Letters. vol. 70, no. 1, pp. 102-104, 1997.

[32] Z. Vardeny and J. Tauc. Picosecond coherence coupling in the pump and probe technique. Optics Communications. vol. 39, no. 6, pp. 396-400, 1981.

[33] S. L Palfrey and T. F. Heinz. Coherent interactions in pump-probe absorption measurements: the effect of phase gratings. Journal of the Optical Society of America B. vol. 2, no. 4, pp. 674-678, 1985.

[34] A. L. Smirl, T. F. Boggess, B. S. Wherrett, G. P. Perryman, and A. Miller. Picosecond transient orientational and concentration gratings in Germanium. IEEE Journal of Quantum Electronics. vol. 19, no. 4, pp. 690-700, 1983.

[35] J. Mørk and A. Mecozzi. Response function for gain and refractive index dynamics in active semiconductor waveguides. Applied Physics Letters. vol. 65, no. 14, pp. 1736-1738, 1994.

[36] A. Mecozzi and J. Mørk. Theory of heterodyne pump-probe experiments with femtosecond pulses. Journal of the Optical Society of America B. vol. 13, no. 11, pp. 2437-2452, 1996.

[37] J. Mørk and A. Mecozzi. Response function for gain and refractive index dynamics in active semiconductor waveguides. Applied Physics Letters. vol. 65, no. 14, pp. 1736-1738, 1994.

[38] J. Mørk and A. Mecozzi. Theory of the ultrafast optical response of active semiconductor waveguides. Journal of the Optical Society of America B. vol. 13, no. 8, pp. 1803-1816, 1996.

[39] J. Mørk, A. Mecozzi, and C. Hultgren. Spectral effects in short pulse pump-probe experiments. Applied Physics Letters. vol. 68, no. 4, pp. 449-451, 1996.

[40]   J. Mark, L. Y. Liu, K. L. Hall, H. A. Haus, and E. P. Ippen. Femtosecond pulse generation in a laser with a nonlinear external resonator. Optics Letter. vol. 14, pp. 48-50, January 1989.

[41]   L. F. Mollenauer. Color Center Lasers. Laser Handbook. pp. 143-228, Elsevier Science Publishers B. V., 1985.

[42]   F. M. Mitschke and L. F. Mollenauer. Stabilizing the soliton laser. IEEE Journal of Quantum Electronics. vol. 22, pp. 2242-2250, 1986.

[43]   I. N. Duling. Subpicosecond all-fibre erbium lasers. Electronics Letters. vol. 27, pp 544-545, 1991.

[44]   M. E. Fermann, K. Sugden, and I Bennion. Generation of 10 nJ picosecond pulses from a modelocked fibre laser. Electronics Letters. vol. 31, pp 194-195, 1995.

[45]   K. Tamura, E. P. Ippen, H. A. Haus, and L. E. Nelson. 77-fs pulse generation from a stretched-pulse mode-locked all-fiber ring laser. Optics Letters. vol. 18, no. 13, pp. 1080-1082, 1993.

[46]   K. Tamura, L. E. Nelson, H. A. Haus, and E. P. Ippen. Soliton versus nonsoliton operation of fiber ring lasers. Applied Physics Letters. vol. 64, no. 2, pp. 149-151, 1994.

[47]   K. Tamura, C. R. Doerr, L. E. Nelson, H. A. Haus, and E. P. Ippen. Technique for obtaining high-energy ultrashort pulses from an additive-pulse mode-locked erbium-doped fiber ring laser. Optics Letters. vol. 19, pp 46-48, 1994.

[48]   G. Lenz, K. Tamura, H. A. Haus, and E. P. Ippen. All-solid--state femtosecond source at 1.55 μm. Optics Letters. vol. 20, pp. 1289-1291, 1995.

[49]   L. E. Nelson, S. B. Fleischer, G. Lenz, and E. P. Ippen. Efficient frequency doubling of a femtosecond fiber laser. Optics Letters. vol. 21, no. 21, pp. 1759-1761, 1996.

[50]   O. E. Martinez, J. P. Gordon, and R. L. Fork. Negative group-velocity dispersion using refraction. Journal of the Optical Society of America A. vol. 1, no. 10, pp. 1003-1006, 1984.

[51]   K. Tamura, M. Nakazawa. Optimizing power extraction in stretched-pulse fiber ring lasers. Applied Physics Letters. vol. 67, no. 25, pp. 3691-3693, 1995.

[52]   P. E. Powers, R. J. Ellingson, W. S. Pelouch, and C. L. Tang. Recent advances of the Ti:Sapphire-pumped high-repetition-rate femtosecond optical parametric oscillator. Journal of the Optical Society of America B. vol. 10, pp. 2162-2167, 1993.

[53]   R. R. Alfano, ed. The Supercontinuum Laser Source. Springer Verlag, New York, 1989.

[54]   A. Sennaroglu, C. R. Pollock, and H. Nathel. Continuous-wave self-modelocked operation of a femtosecond Cr^{+4}:YAG laser. Optics Letters. vol. 19, pp. 390-392, 1994.

[55]   K. L. Hall, G. Lenz, E. P. Ippen, and G. Raybon. Heterodyne pump-probe technique for time-domain studies of optical nonlinearities in waveguides. Optics Letters. vol. 17, no. 12, pp. 874-876, 1992.

[56]   K. L. Hall, A. M. Darwish, E. P. Ippen, U. Koren, and G. Raybon. Femtosecond index nonlinearities in InGaAsP optical amplifiers. Applied Physics Letters. vol. 62, no. 12, pp. 1320-1322, 1993.

[57]   C.-K. Sun, H. K. Choi, C. A. Wang, and J. G. Fujimoto. Femtosecond gain dynamics in InGaAs/AlGaAs strained-layer single-quantum-well diode lasers. Applied Physics Letters. vol. 65, no. 1, pp. 96-98, 1993.

[58]   C.-K. Sun, B. Golubovic, H. K. Choi, C. A. Wang, and J. G. Fujimoto. Femtosecond investigation of spectral hold burning in semiconductor lasers. Applied Physics Letters. vol. 66, no. 13, pp. 1650-1652, 1995.

[59]   K. L. Hall, E. P. Ippen, and G. Eisenstein. Bias-lead monitoring of ultrafast nonlinearities in InGaAsP diode laser amplifiers. Applied Physics Letters. vol. 57, no. 2, pp. 129-131, 1990.

[60]   K. L. Hall, Y. Lai, E. P. Ippen, G. Eisenstein, and U. Koren. Femtosecond gain dynamics and saturation behavior in InGaAsP multiple quantum well optical amplifiers. Applied Physics Letters. vol. 57, no. 31, pp. 2888-2890, 1990.

[61] Y. Lai, K. L. Hall, E. P. Ippen, and G. Eisenstein. Short pulse gain saturation in InGaAsP diode laser amplifiers. IEEE Photonics Technology Letters. vol. 2, no. 10, pp.711-713, 1990.

[62] G. Lenz, E. P. Ippen, J. M. Wiesenfeld, M. A. Newkirk, and U. Koren. Femtosecond dynamics of the non-linear anisotropy in polarization insensitive semiconductor optical amplifiers. Applied Physics Letters. vol. 68, no. 21, pp. 2933-2935, 1996.

[63] C. T. Hultgren and E. P. Ippen. Ultrafast refractive index dynamics in AlGaAs diode laser amplifiers. Applied Physics Letters. vol. 59, no. 6, pp. 635-637, 1991.

[64] C. T. Hultgren, D. J. Dougherty, and E. P. Ippen. Above- and below-band femtosecond nonlinearities in active AlGaAs waveguides. Applied Physics Letters. vol. 61, no.23, pp. 2767-2769, 1992.

[65] K. L. Hall, G. Lenz, and E. P. Ippen. Femtosecond time domain measurements of group velocity dispersion in diode lasers at 1.5 μm. Journal of Lightwave Technology. vol. 10, no. 5, pp. 616-619, 1992.

5778- 79